



ANNUAL
REVIEWS **Further**

Click [here](#) to view this article's
online features:

- Download figures as PPT slides
- Navigate linked references
- Download citations
- Explore related articles
- Search keywords

Semiclassical Path Integral Dynamics: Photosynthetic Energy Transfer with Realistic Environment Interactions

Mi Kyung Lee,¹ Pengfei Huo,² and David F. Coker¹

¹Department of Chemistry, Boston University, Boston, Massachusetts 02215;
email: coker@bu.edu

²Department of Chemistry, University of Rochester, Rochester, New York 14627;
email: pengfei.huo@rochester.edu

Annu. Rev. Phys. Chem. 2016. 67:639–68

First published online as a Review in Advance on
April 18, 2016

The *Annual Review of Physical Chemistry* is online at
physchem.annualreviews.org

This article's doi:
10.1146/annurev-physchem-040215-112252

Copyright © 2016 by Annual Reviews.
All rights reserved

Keywords

semiclassical dynamics, path integral, coherent exciton dynamics, light
harvesting systems, electron–phonon coupling, spectral density

Abstract

This article reviews recent progress in the theoretical modeling of excitation energy transfer (EET) processes in natural light harvesting complexes. The iterative partial linearized density matrix path–integral propagation approach, which involves both forward and backward propagation of electronic degrees of freedom together with a linearized, short-time approximation for the nuclear degrees of freedom, provides an accurate and efficient way to model the nonadiabatic quantum dynamics at the heart of these EET processes. Combined with a recently developed chromophore–protein interaction model that incorporates both accurate ab initio descriptions of intracomplex vibrations and chromophore–protein interactions treated with atomistic detail, these simulation tools are beginning to unravel the detailed EET pathways and relaxation dynamics in light harvesting complexes.

1. INTRODUCTION

Photosynthetic systems (1) that involve assemblies of many chromophores embedded in protein scaffoldings function as extraordinarily efficient solar energy capture and transfer devices that funnel electronic excitation into reaction centers. Understanding the basic dynamical processes of excitation energy transfer (EET) through accurate simulations may enable the design of new nanostructured materials and devices capable of efficient capture and utilization of light. In this review, we discuss the recent theoretical progress in pursuing this goal, with emphasis on the development of accurate dynamical simulation methods that can describe EET dynamics across a broad range of parameter regimes, as well as computational techniques that can be used to construct reliable model Hamiltonians that incorporate *ab initio* accuracy with atomistic detail.

Recent multidimensional nonlinear spectroscopic experiments have been interpreted as suggesting that the early stages of EET processes involve long-lived quantum coherent superpositions of the excitonic states (2–16) that evolve into incoherent mixtures as a result of dissipative energy transfer dynamics (4, 5). These interpretations have produced interesting discussions in the literature on the origins of coherent beating (17–26) and on the possible roles that such coherence might play in facilitating EET efficiency (27–32). Accurate and efficient dynamical methods and simulation techniques are required in order to reliably describe these EET dynamics because of the complexity of the dynamical process itself as well as the complex structure of pigment–protein light harvesting systems (2, 29, 33).

Accurately propagating EET dynamics in these light harvesting systems brings significant challenges to traditional theoretical methods (34). Electronic and pigment–protein couplings often exhibit a broad range of different parameter regimes in these systems, whereas the traditional analytical theories, such as Förster resonance energy transfer (FRET) theory (35–37) and approaches based on the Redfield equations (38), are only valid in particular regimes, so applying them in general to these systems can lead to complications (38, 39). The relatively long-lived solvent response (memory effects from the protein and solvation environment) in these systems also can make the Markovian assumption at the heart of the Redfield and Lindblad master equation approaches problematic for applications to this general class of systems (38, 40–43). Considerable effort has been devoted to developing numerically exact methods (44–51) as well as approximate approaches based on mixed quantum–classical ideas (52, 53) or on the polaron transformed master equation (54–57). However, reducing computational cost (58, 59), incorporating the capability to treat general Hamiltonians (54–57, 59), and achieving accurate dynamics at long times (53, 60–62) remain significant challenges for these methods.

Constructing realistic model Hamiltonians for which the quantum dynamics can be accurately simulated and which capture the essential physics governing the dynamics of these complex systems, in particular the exciton–phonon interaction, remains another central challenge in this field (63). Despite the recent progress in *ab initio* on-the-fly propagation of EET dynamics (64), the most widely used computational strategy for parameterizing these models currently involves performing ground-state classical molecular dynamics (MD) simulations using molecular mechanics (MM) force fields to sample the configurational fluctuations of the chromophores and their protein environment, and then post-processing these MM configurations using semiempirical (65, 66) or density functional theory (DFT) electronic structure calculations (67) to extract the excitation energy fluctuation correlation function averaged along the precomputed trajectory (68–72). However, applying electronic structure calculations for these presampled configurations that explore regions around the local minima of the MM force field can provide unreliable estimates of the magnitude of the excitation energy fluctuations because of the mismatch of the vibrational motion frequencies in the local minima of the MM force field and the *ab initio* quantum mechanical (QM) potential surfaces (73–76).

Here we review recent theoretical progress addressing both of these challenges. First, we briefly outline the partial linearized density matrix (PLDM) approach that, as we demonstrate, can provide a systematically improvable, accurate, and flexible numerical propagation scheme for treating EET dynamics in a wide variety of natural photosynthetic light harvesting systems (77–79). Next, we present a recently developed simulation protocol that separately calculates the intrachromophore vibrational contribution and the intermolecular protein environment component of the exciton–phonon coupling in these pigment–protein complex systems (80–82). With both quantum mechanical calculations for intramolecular vibrations and all-atomistic simulations that realistically account for low-frequency collective motions of intermolecular pigment–protein interactions, this approach can provide an accurate representation of spectral density, a key quantity that describes exciton–vibrational interactions. We demonstrate the reliability of this new approach in benchmark studies that compare calculation results with detailed experimental spectroscopic measurements of the frequency dependence of electron–phonon coupling in the Fenna–Matthews–Olson (FMO) photosynthetic EET complex. Finally, we show how the accurate general-purpose linearized dynamics approach can be implemented together with this realistic description of the interactions in these pigment–protein complexes, enabling reliable simulation studies of EET processes.

2. PARTIAL LINEARIZED DENSITY MATRIX PATH-INTEGRAL PROPAGATION

In this section, we outline a theoretical approach that has been recently developed and successfully applied to propagating the quantum dynamics of large multichromophore pigment–protein complexes, and has been specifically used in studies of EET dynamics in such systems. We are interested in the evolution of the density matrix describing a system of nuclei with positions, R , coupled to an electronic subsystem with states labeled by quantum numbers, n , so that the composite system at time t is described by states $|R_t n_t\rangle$ and the density matrix in terms of these states evolves as

$$\langle R_t n_t | \hat{\rho}(t) | R'_t n'_t \rangle = \sum_{n_0, n'_0} \int dR_0 dR'_0 \langle R_t n_t | e^{-(i/\hbar)\hat{H}t} | R_0 n_0 \rangle \langle R_0 n_0 | \hat{\rho}(0) | R'_0 n'_0 \rangle \langle R'_0 n'_0 | e^{(i/\hbar)\hat{H}t} | R'_t n'_t \rangle, \quad (1)$$

where the total Hamiltonian is written as the nuclear kinetic energy plus the potential energy for the different electronic states and the electronic coupling between these states that depend on nuclear configuration, $\hat{H} = \hat{T} + \sum_{\alpha, \gamma} |\alpha\rangle\langle\alpha| \hat{b}_{\text{el}}(\hat{R}) |\gamma\rangle\langle\gamma|$. Here, for example, \hat{R} represents the degrees of freedom (DOFs) of the protein scaffold, the solvent, and the vibrations of the chromophores. In applications to energy transfer in pigment–protein complexes, it is often useful to work in a diabatic representation in which the quantum subsystem states, $|\alpha\rangle$, represent electronic excitations localized on particular chromophores in a Frenkel exciton model (for the derivation and implementation of the current theory in the adiabatic representation, see Reference 79). The density matrix expression in Equation 1 contains two propagators, one forward and one backward, each of which has both electronic and nuclear DOFs.

The approach outlined here aims to express both propagators in terms of a nuclear phase space path-integral formalism and then to apply a linearization approximation based on the smallness of the difference between the forward and backward paths of these “heavy” nuclear DOFs. For the “light” electronic DOFs, however, this approach retains both forward and backward amplitudes and so includes important electronic interference effects between these different amplitudes. By doing this, we achieve a more accurate description of the electronic dynamics compared to fully linearized methods such as linearized semiclassical initial value representation (LSC-IVR) (83–85)

and the Poisson bracket mapping equation (PBME) (86, 87); at the same time, we reduce the computational costs through the partial linearization treatment of the nuclear DOFs. Compared to the usual master equation approaches used to explore EET, this partial linearized approach is nonperturbative, does not require making the Markovian approximation, and does not require any particular form for the Hamiltonian.

Below, we briefly outline the derivation of this approach. We start by introducing the mapping representation, and then we rewrite the forward and backward propagators in terms of the path-integral formalism. With a partial linearization in terms of the nuclear path difference, we derive the PLDM formalism and the corresponding equations of motion. Finally, we discuss the iterative implementation of PLDM propagation.

2.1. Mapping Representation

In order to put both electronic and nuclear DOFs on the same dynamical footing and to obtain a continuous path-integral expression for both sets of DOFs, we follow the mapping approach (88–91) that replaces the evolution of the electronic subsystem by the dynamics of a set of fictitious mapping harmonic oscillators whose motion is restricted to remain in the single excitation subspace.

Following the seminal papers of Stock & Thoss (88, 89), Miller & McCurdy (90), and Meyer & Miller (91), the quantum amplitude transfer operator and the various terms in the electronic Hamiltonian operator are written in terms of bosonic raising and lowering operators as

$$|\alpha\rangle\langle\gamma| \rightarrow \hat{a}_\alpha^\dagger \hat{a}_\gamma, \quad |\alpha\rangle\langle\alpha|\hat{b}_{\text{el}}(\hat{R})|\gamma\rangle\langle\gamma| \rightarrow \langle\alpha|\hat{b}_{\text{el}}(\hat{R})|\gamma\rangle\hat{a}_\alpha^\dagger \hat{a}_\gamma, \quad (2)$$

where these operators can be expressed in terms of Cartesian coordinates and momenta of individual oscillators (one for each electronic state) as $\hat{a}_\gamma = (1/\sqrt{2\hbar})(\hat{q}_\gamma - i\hat{p}_\gamma)$ and $\hat{a}_\gamma^\dagger = (1/\sqrt{2\hbar})(\hat{q}_\gamma + i\hat{p}_\gamma)$. Thus, the electronic Hamiltonian in the diabatic representation,¹ $\hat{b}_{\text{el}}(\hat{R}) = \sum_{\alpha,\gamma} |\alpha\rangle\langle\alpha|\hat{b}_{\text{el}}(\hat{R})|\gamma\rangle\langle\gamma|$, can be rewritten in this mapping formulation as

$$\hat{b}_m(\hat{R}) = \frac{1}{2\hbar} \sum_{\alpha} b_{\alpha,\alpha}(\hat{R})(\hat{q}_\alpha^2 + \hat{p}_\alpha^2 - \hbar) + \frac{1}{2\hbar} \sum_{\gamma \neq \alpha} b_{\alpha\gamma}(\hat{R})(\hat{q}_\alpha \hat{q}_\gamma + \hat{p}_\alpha \hat{p}_\gamma), \quad (3)$$

where \hat{P} , \hat{R} and \hat{p} , \hat{q} represent the nuclear and mapping phase space DOFs, respectively, and we have made use of the boson commutation relation, $[\hat{q}_\alpha, \hat{p}_\gamma] = i\hbar\delta_{\alpha\gamma}$, satisfied by the mapping oscillator variables.

2.2. Path-Integral Formalism for the Mapping Propagator

Now we use the path-integral formalism to write the propagators that appear in the expression for the density matrix evolution in Equation 1.

The propagator matrix elements can thus be written in discrete phase space path-integral form as

$$\langle R_N n_t | e^{-(i/\hbar)\hat{H}t} | R_0 n_0 \rangle = \int \prod_{k=1}^{N-1} dR_k \frac{dP_k}{2\pi\hbar} \frac{dP_N}{2\pi\hbar} e^{(i/\hbar)S_0} T_{[n_t, n_0]}, \quad (4)$$

¹The mapping approach in the adiabatic representation can also be derived with careful consideration of the derivative coupling vector. The detailed derivation and numerical implementation can be found in References 79, 127, and 128.

where

$$S_0 = \epsilon \sum_{k=1}^N \left[P_k \frac{(R_k - R_{k-1})}{\epsilon} - \frac{P_k^2}{2M} \right]$$

is the nuclear kinetic action and $T_{[n_t, n_0]} = \langle n_t | e^{-(i/\hbar)\epsilon \hat{h}_m(R_{N-1})} \dots e^{-(i/\hbar)\epsilon \hat{h}_m(R_0)} | n_0 \rangle$ is the quantum transition amplitude associated with the evolution of the mapping Hamiltonian $\hat{h}_m(\hat{R}_t)$ along the discrete path of nuclear configurations, $\{R_t\}$.

We choose the coherent state representation (92, 93) to express the electronic transition amplitude $T_{[n_t, n_0]}$ (setting the coherent state width parameter to $\gamma = \frac{1}{2}$ and choosing units in which $\hbar = 1$) (94–96) so that

$$T_{[n_t, n_0]} = \int dq_0 dp_0 \frac{1}{4} (q_{n_t} + i p_{n_t}) (q_{n_0} - i p_{n_0}) c_t e^{i S_1(t)} e^{-(i/2) \sum_{\alpha} (q_{\alpha t} p_{\alpha t} - q_{\alpha 0} p_{\alpha 0})} e^{-(1/2) \sum_{\alpha} (q_{\alpha 0}^2 + p_{\alpha 0}^2)}. \quad (5)$$

Here, c_t is the prefactor for the mapping semiclassical propagator, and can be further expressed as $c_t = e^{-(i/2\hbar) \int_0^t d\tau \sum_{\alpha} \hat{h}_{\alpha\alpha}(R_{\tau})}$. The action associated with the mapping Hamiltonian is $S_1(t) = \int_0^t L_1(\tau) d\tau$, with $L_1 = \sum_{\alpha} p_{\alpha} \dot{q}_{\alpha} - b_m^{\text{cl}}(R) + \frac{1}{2} \sum_{\alpha} b_{\alpha\alpha}(R)$ and the classical mapping Hamiltonian

$$b_m^{\text{cl}}(R, p, q) = \frac{1}{2} \sum_{\alpha} b_{\alpha\alpha}(R) (p_{\alpha}^2 + q_{\alpha}^2) + \frac{1}{2} \sum_{\gamma \neq \alpha} b_{\gamma\alpha}(R) (p_{\gamma} p_{\alpha} + q_{\gamma} q_{\alpha}). \quad (6)$$

The term $(\hbar/2) \sum_{\alpha} b_{\alpha\alpha}(R)$ in the action, which arises from the original mapping Hamiltonian in Equation 3, exactly cancels² the harmonic prefactor, c_t (94–96).

2.3. Linearization Approximation and the Partial Linearized Density Matrix Formalism

According to Equation 1, the forward and backward propagators must be combined to evolve the density matrix, and this can lead to phase interference in the integrand of the path-integral expression for the density matrix. Accurate representation of such interference effects in numerical implementation often presents problems, especially for those nuclear DOFs whose actions result in highly oscillatory factors. Approximate schemes such as forward–backward semiclassical initial value representation (83, 84, 97) can alleviate these difficulties. Alternatively, to circumvent these problems, here we follow the idea of partial linearization (95, 96, 98–103) in the nuclear DOF that begins by transforming the forward and backward nuclear path variables, R and R' , into mean and difference path variables: $\bar{R} = (R + R')/2$ and $Z = (R - R')$, respectively [with a similar transformation for the nuclear environment momenta, $\bar{P} = (P + P')/2$ and $Y = (P - P')]$. The nuclear kinetic action difference can then be rewritten exactly as

$$(S_0 - S'_0) = \bar{P}_N Z_N - \bar{P}_1 Z_0 - \sum_{k=1}^{N-1} (\bar{P}_{k+1} - \bar{P}_k) Z_k - \sum_{k=1}^N \left[\frac{\epsilon}{m} \bar{P}_k - (\bar{R}_k - \bar{R}_{k-1}) \right] Y_k. \quad (7)$$

The central approximation in this partial linearization approach involves truncating the phase difference in the combined transition amplitude terms to linear order in the path difference variables Y and Z on the assumption that for short times, the forward and backward paths will remain close to each other. Expanding the action difference to first order in the path difference variables and using the approximation that $\sum_{\alpha} p_{\alpha} \dot{q}_{\alpha} - b_m^{\text{cl}}(\bar{R}, p, q) \sim \sum_{\alpha} p_{\alpha} \dot{q}_{\alpha} - b_m^{\text{cl}}(R, p, q) =$

²This brings additional benefits because the $(\hbar/2) \sum_{\alpha} b_{\alpha\alpha}(R)$ term can cause the potential to be inverted. Further, the population $\rho_{\alpha\alpha} \sim (q_{\alpha t}^2 + p_{\alpha t}^2)$ is now guaranteed to be positive with this formulation.

$\frac{1}{2}(\mathrm{d}/\mathrm{d}\tau)(\sum_{\alpha} p_{\alpha} q_{\alpha})$ to first order in the path difference, we find that the transition amplitude phase can be rewritten as

$$(S_1 - S'_1) = \int_0^t \mathrm{d}\tau \frac{1}{2} \frac{\mathrm{d}}{\mathrm{d}\tau} \sum_{\alpha} (p_{\alpha\tau} q_{\alpha\tau} - p'_{\alpha\tau} q'_{\alpha\tau}) \quad (8)$$

$$+ \int_0^t \mathrm{d}\tau \left[\frac{1}{2} \nabla_{\bar{R}} \left(b_m^{\mathrm{cl}}(\bar{R}_{\tau}, p_{\tau}, q_{\tau}) + b_m^{\mathrm{cl}}(\bar{R}_{\tau}, p'_{\tau}, q'_{\tau}) \right) Z_{\tau} + \mathcal{O}(Z_{\tau}^2) \right].$$

With this expression, the first term in Equation 8 cancels the boundary terms in $T_{[n_t, n_0]}$ given in Equation 5, with similar cancellation in the backward path transition amplitude, $T'_{[n'_0, n'_t]}$.

Combining these approximate forward and backward phase factors ($e^{i/\hbar(S_0 - S'_0)} T_{[n_t, n_0]} T'_{[n'_0, n'_t]}$) and performing the analytic integrals over the difference variables $Z_0 \dots Z_{N-1}$ and $Y_1 \dots Y_N$, which yield δ -functions in terms of the mean variables in the resulting partial linearized expression for the evolving density matrix, we arrive at the final approximate expression for the elements of $\rho(t)$:

$$\left\langle \bar{R}_N + \frac{Z_N}{2} n_t \mid \hat{\rho}(t) \mid \bar{R}_N - \frac{Z_N}{2} n'_t \right\rangle = \sum_{n_0, n'_0} \int \mathrm{d}\bar{R}_0 \mathrm{d}q_0 \mathrm{d}p_0 \mathrm{d}q'_0 \mathrm{d}p'_0 G_0 G'_0 \Gamma_{[n_t, n'_t]} \Gamma_{[n_0, n'_0]}^* \quad (9)$$

$$\times \prod_{k=1}^{N-1} \int \mathrm{d}\bar{R}_k \frac{\mathrm{d}\bar{P}_N}{2\pi\hbar} (\hat{\rho})_{W}^{n_0, n'_0}(\bar{R}_0, \bar{P}_1) e^{(i/\hbar)\bar{P}_N Z_N} \delta \left[\frac{\bar{P}_{k+1} - \bar{P}_k}{\epsilon} - F_k \right] \prod_{k=1}^N \frac{\mathrm{d}\bar{P}_k}{2\pi\hbar} \delta \left[\frac{\bar{P}_k}{M} - \frac{\bar{R}_k - \bar{R}_{k-1}}{\epsilon} \right].$$

Here we have collected the endpoint polynomial factors as, for example, $\Gamma_{[n_t, n'_t]} = \frac{1}{4}(q_{n_t} + ip_{n_t})(q'_{n'_t} + ip'_{n'_t})$, and defined $G_0 = e^{-(1/2)\sum_{\alpha}(q_{\alpha 0}^2 + p_{\alpha 0}^2)}$ and $G'_0 = e^{-(1/2)\sum_{\alpha'}(q_{\alpha' 0}^2 + p_{\alpha' 0}^2)}$, which provide the initial distributions for the forward and backward mapping variables. In this expression, the initial distribution of the mean nuclear DOF is determined by the partial Wigner transform of the initial density with respect to the bath variables

$$(\hat{\rho})_W^{n_0, n'_0}(\bar{R}_0, \bar{P}_1) = \int \mathrm{d}Z_0 \left\langle \bar{R}_0 + \frac{Z_0}{2} n_0 \mid \hat{\rho} \mid \bar{R}_0 - \frac{Z_0}{2} n'_0 \right\rangle e^{-(i/\hbar)\bar{P}_1 Z_0}. \quad (10)$$

This partial linearization procedure approximates the forward and backward path-integral kernel as a product of sequential δ -functions, so according to Equation 9, the time evolving density matrix can be computed by employing classical-like trajectories that are propagated using the following equations of motion and effective classical mean path force:

$$\dot{q}_{n_t} = \frac{\partial b_m^{\mathrm{cl}}(\bar{R}_t)}{\partial p_{n_t}}, \quad \dot{p}_{n_t} = -\frac{\partial b_m^{\mathrm{cl}}(\bar{R}_t)}{\partial q_{n_t}};$$

$$F_k = -\frac{1}{2} [\nabla_{\bar{R}_k} b_m^{\mathrm{cl}}(\bar{R}_k, p_k, q_k) + \nabla_{\bar{R}_k} b_m^{\mathrm{cl}}(\bar{R}_k, p'_k, q'_k)]. \quad (11)$$

Numerical implementation of these expressions is straightforward, and it includes sampling initial values of the nuclear DOF from $(\hat{\rho})_W^{n_0, n'_0}(\bar{R}_0, \bar{P}_1)$; the mapping variables are sampled from initial Gaussian distributions. The product of δ -functions in Equation 9 is equivalent to a time-stepping prescription for the evolution of the bath variables.

Applying a simple canonical transformation shows that the above results are equivalent to an extended system of Hamilton's equations. This result has recently been derived from a completely different formal point of view, starting from the mixed quantum-classical Liouville equation (104–106).

Finally, we note that with the partially linearized propagation result in Equation 9, it is simple to compute expectation values or correlation functions of arbitrary operators at a given time (129). Applying the definition of a Wigner transform in Equation 10 to the PLDM propagated density

matrix in Equation 9,

$$(\hat{\rho})_{W}^{n_t, n'_t}(\bar{R}_N, \bar{P}_{N+1}, t) = \int dZ_N \left\langle \bar{R}_N + \frac{Z_N}{2} n_t \left| \hat{\rho}(t) \right| \bar{R}_N - \frac{Z_N}{2} n'_t \right\rangle e^{-(i/\hbar) \bar{P}_{N+1} Z_N}, \quad (12)$$

we see clearly that when the phase factor $e^{(i/\hbar) \bar{P}_N Z_N}$ that weights each trajectory's contribution to the propagated result in Equation 9 is combined with the factor $e^{-(i/\hbar) \bar{P}_{N+1} Z_N}$ from the Wigner transformed result in Equation 12, the Wigner transform integral over Z_N results in a $\delta(\bar{P}_N - \bar{P}_{N+1})$, so the phase space distribution associated with the Wigner transformed density matrix at time t can be simply evaluated by binning a weighted histogram of the final phase space points of our ensemble of trajectories.

2.4. Iterative Propagation Schemes

The linearized approximation on which the PLDM formalism is based is generally accurate for short times, during which the forward and backward nuclear paths deviate little from each other. As we see in some of the numerical examples presented in Section 5.1, the PLDM approximation can generate inaccurate results for long times despite its great accuracy at short times. Here we provide a theoretical framework that can systematically improve the accuracy of the long-time propagation for general systems based on the iterative implementation of the short-time linearization approximation (79, 107).

In this scheme, we apply the linearized approximation for a series of short-time propagations that are concatenated by employing resolutions of the identity in which the intervening sums over states are implemented through a Monte Carlo sampling procedure, and integrations over nuclear phase space variables are done analytically; this gives accurate density matrix propagation for a full, longer time interval.

In the result below, for example, the propagation of the density matrix out to time $2t$ can be expressed in terms of two shorter time propagations, each of time t in duration:

$$\langle R_{2t} n_{2t} | \hat{\rho}(2t) | R'_{2t} n'_{2t} \rangle = \sum_{n_t, n'_t} \int dR_t dR'_t \langle R_{2t} n_{2t} | e^{-(i/\hbar) \hat{H} t} | R_t n_t \rangle \langle \hat{\rho}(t) \rangle \langle R'_t n'_t | e^{(i/\hbar) \hat{H} t} | R'_{2t} n'_{2t} \rangle. \quad (13)$$

Here the first propagation to time t , implicit in the term $\langle \hat{\rho}(t) \rangle = \langle R_t n_t | \hat{\rho}(t) | R'_t n'_t \rangle$, is performed using the linearization approximation in Equation 9. The above result is identical to Equation 1, with the time propagation interval shifted from $0 \rightarrow t$ to $t \rightarrow 2t$. Applying the same linearization ideas that lead from Equation 1 to Equation 9 in the context of the above result yields the iterative time segment concatenation scheme. In particular, as indicated in Equation 12, the partial linearized propagation from 0 to t produces an ensemble of trajectory phase space endpoints and mapping variables distributed according to $(\hat{\rho})_{W}^{n_t, n'_t}(\bar{R}_N, \bar{P}_{N+1}, t)$. These provide initial conditions for the evolution of the next time segment, $t \rightarrow 2t$, just as the initial Wigner density $(\hat{\rho})_{W}^{n_0, n'_0}(\bar{R}_0, \bar{P}_1)$ had to be sampled according to Equation 1 to initialize propagation of the system over the first time segment, $0 \rightarrow t$. As outlined above Equation 9, integrals over the nuclear endpoint difference variables produce a δ -function that makes the nuclear momentum continuous from the end of the first segment to the beginning of the next. Also, the coordinate δ -function in the integrand in Equation 9, generalized to the $t \rightarrow 2t$ interval, which reads $\delta[\bar{P}_{N+1}/M - (\bar{R}_{N+1} - \bar{R}_N)/\epsilon]$, enables integration over the first nuclear configuration in the new segment; i.e., one performs the $\int d\bar{R}_N$ and analytically completes the connection between the previous segments of the mean path variables to start the new segment.

The final ingredient of our iterative scheme starts by using the electronic amplitudes from the end of the previous time segment, i.e., the products of polynomials, $\Gamma_{[n_t, n'_t]}$, to estimate the

electronic density matrix at time t along the current trajectory. As detailed in References 79 and 107, the magnitudes of the local electronic density matrix elements for this trajectory are used to define a normalized Monte Carlo sampling distribution that is employed to stochastically resolve the trajectory into one of the competitive density matrix elements, and this importance sampled density matrix element is used to define the new electronic subsystem initial condition for the propagation of the next short-time segment of dynamics. This Monte Carlo intermediate initial state sampling thus performs the sums over the starting states of the new propagation segment; i.e., the $\sum_{n_t} \sum_{n'_t}$ are used in the same fashion as the zero time state sums in Equation 9. Finally we perform the integrals over the coherent state mapping variable distribution for the new time step, i.e., $\int dq_t dp_t dq'_t dp'_t G_t G'_t$, using a steepest descent approximation called focusing that is outlined in References 94, 95, and 96. By this approximation, one selects a single initial condition from the peak of the Gaussian hermite polynomial product distribution of occupied density matrix elements.

We refer to this Monte Carlo implementation of Equation 13 as the iterative partial linearized density matrix (IPLDM) approach (79, 107). With more iterations for a given propagation time, the accuracy can be systematically improved through this approach, but the numerical cost increases rapidly with the number of iterations (79), as results at longer times have statistical fluctuations. This implementation, however, does offer the possibility to systematically improve results, and provides the ability to balance accuracy and computational costs for practical applications.

3. REALISTIC MODELING OF SYSTEM-BATH INTERACTIONS

3.1. Model Hamiltonian

The model Hamiltonian often used to describe pigment–protein light harvesting complexes is of the Frenkel exciton tight-binding system–bath form (108)

$$\hat{H} = \hat{H}_s + \hat{H}_{sb}, \quad (14)$$

in which the system part contains the single excitation states as well as transition dipole coupling terms between states in which electronic excitation is localized on different chromophores:

$$\hat{H}_s = \sum_{\alpha=1}^N \epsilon_{\alpha} |\alpha\rangle \langle \alpha| + \sum_{\alpha \neq \gamma}^N \Delta_{\alpha,\gamma} |\alpha\rangle \langle \gamma|. \quad (15)$$

Here the state $|\alpha\rangle$ represents the localized excitation of a single chromophore of the multichromophore system. In this state, chromophore α is in its first excited state and all other chromophores remain in their ground states. The quantity ϵ_{α} is the excitation energy of chromophore α in the pigment–protein complex, and $\Delta_{\alpha,\gamma}$ is the transition dipole coupling between the different singly excited states. These couplings can be written in the point dipole approximation as $\Delta_{\alpha,\gamma} \sim \kappa |\mu_{\alpha}| |\mu_{\gamma}| / 4\pi\epsilon_0 R^3$, with R the separation between the centers of the chromophores α and γ , $|\mu_{\alpha}| = |\langle \Psi_{\alpha}^e | \hat{\mu} | \Psi_{\alpha}^g \rangle|$ the magnitude of the transition dipole vector matrix element of the donor, and the geometric factor $\kappa = \hat{r}_{\alpha} \cdot \hat{r}_{\gamma} - 3(\hat{r}_{\alpha} \cdot \hat{R})(\hat{r}_{\gamma} \cdot \hat{R})$, where \hat{r}_{α} is a unit vector of the transition dipole of the chromophore α .

In practice, accurate site energies, ϵ_{α} , are difficult to compute from first principles but can be estimated using semiempirical or time-dependent density functional theory (TDDFT) electronic structure methods (67, 109–112) or parameterized with experimental values obtained by interpreting and fitting to spectroscopic results (113–117). The off-diagonal terms $\Delta_{\alpha,\gamma}$, approximated as outlined above, can be calculated more accurately, beyond the point dipole approximation, using the transition density cube method (118) or the transition charge approach based on the electrostatic potential method (119).

To incorporate fluctuations of the excitation energies that result in dissipation to a coupled environment (intrachromophore vibrations and the protein scaffold and solvent), the model Hamiltonian includes a system–bath interaction that is assumed to have a linear dependence on both the excited state population and the bath coordinates. The bath of each chromophore α is thus modeled as a collection of independent harmonic modes, described by phase space variables $\{P_{i\alpha}, Q_{i\alpha}\}$, that are bilinearly coupled to the excitation of the chromophore, described by the population operator, $|\alpha\rangle\langle\alpha|$, so the system–bath Hamiltonian has the form

$$\hat{H}_{\text{sb}} = \sum_{\alpha=1}^N \sum_{i\alpha=1}^{n_{\alpha}} \left[\frac{1}{2} (P_{i\alpha}^2 + \omega_{i\alpha}^2 Q_{i\alpha}^2) + c_{i\alpha} Q_{i\alpha} |\alpha\rangle\langle\alpha| \right]. \quad (16)$$

Here, $c_{i\alpha}$ controls the strength of the interaction of excited chromophore α with the i -th mode of its harmonic bath, whose frequency is $\omega_{i\alpha}$. The properties of the system–bath coupling within this model are usually specified in terms of the spectral density, and here we suppose that each chromophore has its own set of independent bath modes and write the spectral density $J_{\alpha}(\omega)$ for chromophore α , which summarizes the frequencies of the modes and their bilinear coupling strengths, as follows:³

$$J_{\alpha}(\omega) \equiv \frac{\pi}{2} \sum_{i\alpha} \frac{c_{i\alpha}^2}{\omega_{i\alpha}} \delta(\omega - \omega_{i\alpha}). \quad (17)$$

Finally, we note that a central assumption underlying this model is that the excited-state radiative lifetime of the isolated chromophore and its local bath is long compared to the relaxation timescale of the bath.

3.2. Simple Harmonic Analysis of Spectral Densities

In this section, we outline the basic relation between the electronic surfaces and the spectral density, with the bilinearly coupled harmonic system–bath model discussed above. In this model, the ground- and excited-state surfaces are supposed to vary with some bath mode coordinate, $Q_{i\alpha}$. In the ground state, the bath mode is assumed to oscillate around $Q_{i\alpha}^g$, and the excited state potential may be shifted spatially so the bath mode oscillates around $Q_{i\alpha}^e$ when the chromophore is electronically excited. For a given chromophore α , we assume that the ground-state, V_{α}^g , and excited-state, V_{α}^e , surfaces are locally harmonic in this chromophore's bath coordinates.

As outlined above, we assume that the electronic structure-generated surfaces $V_{\alpha}^g(\mathbf{Q}_{\alpha})$ and $V_{\alpha}^e(\mathbf{Q}_{\alpha})$ have the same normal mode frequencies and are described by the same normal mode coordinates, \mathbf{Q}_{α} , and that the equilibrium positions are simply shifted from each other, giving rise to the reorganization energy specified below in Equation 20. In general, this a reasonable approximation, the reliability of which has been explored in studies comparing difference fluorescence line narrowing (ΔFLN ; 120, 121) and hole burning spectra (122). Thus, in our generalized model, we assume that the relevant potential surfaces have the following forms:

$$V_{\alpha}^g(\mathbf{Q}_{\alpha}) = \frac{1}{2} \sum_{i\alpha} \omega_{i\alpha}^2 (Q_{i\alpha} - Q_{i\alpha}^g)^2, \quad (18)$$

$$V_{\alpha}^e(\mathbf{Q}_{\alpha}) = \frac{1}{2} \sum_{i\alpha} \omega_{i\alpha}^2 (Q_{i\alpha} - Q_{i\alpha}^e)^2 + E_{\alpha}. \quad (19)$$

³Equation 17 is the standard definition that appears in most texts (123). Alternatively, because the frequencies $\omega_{i\alpha}$ are positive, for formal purposes it is more convenient to define the spectral density as $J_{\alpha}(\omega) \equiv (\pi/2) \sum_{i\alpha} (c_{i\alpha}^2/\omega_{i\alpha}^2) \omega [\delta(\omega - \omega_{i\alpha}) + \delta(\omega + \omega_{i\alpha})]$, which respects the formal property that $J_{\alpha}(\omega)$ is an odd function of frequency, i.e., $J_{\alpha}(\omega) = -J_{\alpha}(-\omega)$ (123).

The key quantities governing the excited-state relaxation after chromophore photoexcitation are the excited-state reorganization energies of the different bath modes of the excited chromophore, λ_{i_α} . These are the energies that the chromophore loses to its harmonic bath oscillators in relaxing from where it is excited at the Franck–Condon point, $Q_{i_\alpha}^g$, a nonequilibrium configuration of the bath on the excited-state potential, to equilibrium on the excited state characterized by bath configuration $Q_{i_\alpha}^e$. With this definition, we see that the reorganization energies are simply related to the properties of the ground- and excited-state potentials according to the following expression:

$$\lambda_{i_\alpha} = \frac{1}{2} \omega_{i_\alpha}^2 (Q_{i_\alpha}^e - Q_{i_\alpha}^g)^2 = S_{i_\alpha} \hbar \omega_{i_\alpha}. \quad (20)$$

The second equality in this result defines the dimensionless Huang–Rhys factor for the bath mode, S_{i_α} , as the number of vibrational quanta, $\hbar \omega_{i_\alpha}$, in the mode of interest that is equivalent to the amount of energy associated with its reorganization energy. The total reorganization energy of chromophore α with this independent harmonic bath model is simply the sum of the individual chromophore bath mode reorganization energies, so $\lambda_\alpha = \sum_{i_\alpha} \lambda_{i_\alpha}$ and $S_\alpha = \sum_{i_\alpha} S_{i_\alpha}$.

Finally, the shifted parabolic shapes of the ground- and excited-state potentials in this model enable us to express the relative energetic difference between ground and excited state as

$$\delta\epsilon_\alpha(Q_{i_\alpha}) = V_\alpha^e(Q_{i_\alpha}) - V_\alpha^g(Q_{i_\alpha}) = \text{constant} - 2\omega_{i_\alpha}^2 (Q_{i_\alpha}^e - Q_{i_\alpha}^g) Q_{i_\alpha}, \quad (21)$$

where the constant equals $E_\alpha + \omega_{i_\alpha}^2 (Q_{i_\alpha}^e - Q_{i_\alpha}^g)^2$. Comparing with Equation 16, we readily identify an expression for the reorganization energies, λ_{i_α} , in terms of the system–bath bilinear coupling constants, c_{i_α} , as

$$\begin{aligned} c_{i_\alpha} &= 2\omega_{i_\alpha}^2 (Q_{i_\alpha}^e - Q_{i_\alpha}^g) = \sqrt{2\lambda_{i_\alpha}} \omega_{i_\alpha} = \sqrt{2\hbar\omega_{i_\alpha} S_{i_\alpha}} \omega_{i_\alpha}, \\ \lambda_{i_\alpha} &= c_{i_\alpha}^2 / 2\omega_{i_\alpha}^2. \end{aligned} \quad (22)$$

With these results, we see that the spectral density in Equation 17 becomes

$$J_\alpha(\omega) = \pi \sum_{i_\alpha} \omega_{i_\alpha} \lambda_{i_\alpha} \delta(\omega - \omega_{i_\alpha}). \quad (23)$$

3.3. Spectral Density and the Energy-Gap Fluctuation Correlation Function

For the model Hamiltonian detailed above, the excitation energy of chromophore α is assumed to vary linearly as a function of the harmonic bath coordinates associated with this chromophore according to the term $\delta\epsilon_\alpha = \sum_{i_\alpha} c_{i_\alpha} Q_{i_\alpha}$. The excitation energy fluctuation correlation function of chromophore α is thus

$$C_\alpha(t) = \langle \delta\epsilon_\alpha(0) \delta\epsilon_\alpha(t) \rangle = \sum_{i_\alpha} c_{i_\alpha}^2 \langle Q_{i_\alpha}(0) Q_{i_\alpha}(t) \rangle, \quad (24)$$

where the angle brackets represent an equilibrium ensemble average over the thermal distribution of the states of this harmonic bath. In addition to the harmonic approximation, the underlying assumption here is the same as that at the heart of the Onsager regression hypothesis, i.e., that the fluctuations that lead to relaxation and dissipation of the electronic excitation energy of the chromophore are the same as those that characterize the ground-state thermal equilibrium. For a quantum description of the independent harmonic chromophore baths, we find that (123)

$$C_\alpha^{\text{qm}}(t) = \frac{\hbar}{2} \sum_{i_\alpha} \frac{c_{i_\alpha}^2}{\omega_{i_\alpha}} \left[\coth\left(\frac{\beta \hbar \omega_{i_\alpha}}{2}\right) \cos(\omega_{i_\alpha} t) - i \sin(\omega_{i_\alpha} t) \right].$$

If the chromophore harmonic baths are assumed to behave classically, however, this excitation energy correlation function has the form

$$C_{\alpha}^{\text{cl}}(t) = \frac{1}{\beta} \sum_{i_{\alpha}} \left(\frac{c_{i_{\alpha}}^2}{\omega_{i_{\alpha}}^2} \right) \cos(\omega_{i_{\alpha}} t). \quad (25)$$

Multiplying these results appropriately by $\cos \omega t$, integrating over time, and using the fact that $\int_{-\infty}^{\infty} dt e^{i\omega t} = 2\pi \delta(\omega)$, we find the central relations between spectral densities and energy fluctuation correlation functions

$$J(\omega) = \frac{2}{\hbar} \tanh\left(\frac{\beta \hbar \omega}{2}\right) \int_0^{\infty} dt \operatorname{Re}[C^{\text{qm}}(t)] \cos \omega t$$

and

$$J(\omega) = \beta \omega \int_0^{\infty} dt C^{\text{cl}}(t) \cos \omega t. \quad (26)$$

Because quantum correlation functions are generally very difficult to compute for large complex systems, the approach usually adopted is to compute classical equilibrium correlation functions of the excitation energy fluctuations of the chromophores using MD simulations. These are then processed using the classical transformation in Equation 26 so that the classical simulations used to parameterize the environmental interactions and the system–bath model are consistent. Using the quantum relation to compute the spectral density with a classical correlation function leads to an unphysical temperature dependence (67, 70) for the spectral density because of the inconsistent description between the correlation function (classical) and the transformation relation (quantum) (80).

4. HYBRID FIRST PRINCIPLES COMPUTATION OF INTERMOLECULAR AND INTRACHROMOPHORE SPECTRAL DENSITY CONTRIBUTIONS

The spectral density can be readily obtained from cosine transformation of the excitation energy fluctuation correlation function based on Equation 26. Most theoretical studies use a two-stage calculation (75, 76): First, an equilibrium MD simulation is performed to sample the trajectory using a model ground-state MM force field. Next, post-processing calculations that compute the time-dependent excitation energy fluctuations are conducted for snapshot configurations along the trajectory and the correlation function is averaged over different segments of the trajectory, assuming ergodicity. The main potential problem (73) with this commonly used strategy is that the dynamics that determines the component frequencies in the correlation function is generated using a MM force field that drives the MD trajectory, and there is no guarantee that the MM potential accurately resembles the ground-state surface obtained from electronic structure calculations, particularly for all important motions that influence the excitation energy.

To address this issue, we adopt a strategy for computing spectral densities that has been widely used in the description of outer-sphere and inner-sphere electron transfer (123). The basic idea is to decompose the interactions that affect the chromophore excitation energies into short-range, chemical bonding–like intrachromophore terms and longer-range interactions that account for how the environment interacts differently with the ground- and excited-state charge distributions of the chromophore to influence its excitation energy. This strategy suggests that the total spectral density of a given chromophore, α , can be decomposed into two parts,

$$J_{\alpha}(\omega) = J_{\alpha}^{\text{vib}}(\omega) + J_{\alpha}^{\text{inter}}(\omega), \quad (27)$$

where $J_{\alpha}^{\text{vib}}(\omega)$ contains all of the intrachromophore vibrational contributions and $J_{\alpha}^{\text{inter}}(\omega)$ accounts for the intermolecular contributions to excitation energy fluctuations caused by the environment, including how protein and solvent interactions influence the chromophore excitation energy.

As described above, we divide the excitation energy fluctuation $\delta\epsilon_{\alpha}(t)$ appearing in Equation 24 into short- and long-range contributions; thus

$$\delta\epsilon_{\alpha}(t) = \delta\epsilon_{\alpha}^{\text{sr}}(t) + \delta\epsilon_{\alpha}^{\text{lr}}(t). \quad (28)$$

Forming the correlation function as in Equation 24 results in direct terms, as well as cross-terms, of the form $\langle\delta\epsilon_{\alpha}^{\text{sr}}(0)\delta\epsilon_{\alpha}^{\text{lr}}(t)\rangle$ and $\langle\delta\epsilon_{\alpha}^{\text{lr}}(0)\delta\epsilon_{\alpha}^{\text{sr}}(t)\rangle$. If we assume that the excitation energy fluctuations owing to short- and long-range interactions are uncorrelated, these cross-terms vanish on average, and the correlation function we need can be written as the sum of the two direct terms:

$$C_{\alpha}(t) = \langle\delta\epsilon_{\alpha}^{\text{sr}}(0)\delta\epsilon_{\alpha}^{\text{sr}}(t)\rangle + \langle\delta\epsilon_{\alpha}^{\text{lr}}(0)\delta\epsilon_{\alpha}^{\text{lr}}(t)\rangle. \quad (29)$$

Performing the cosine transform as indicated in Equation 26 gives that the spectral densities can be computed as the sum of short- and long-range contributions in this situation, as suggested in Equation 27, thus identifying $J_{\alpha}^{\text{vib}}(\omega)$ with the short-range fluctuation correlation function $\langle\delta\epsilon_{\alpha}^{\text{sr}}(0)\delta\epsilon_{\alpha}^{\text{sr}}(t)\rangle$, and $J_{\alpha}^{\text{inter}}(\omega)$ with the long-range contribution.

The approach outlined here assumes separations of both time and length scales. Thus, the intrachromophore vibrations are supposed to take place in an ensemble of distorted potentials, the characteristics of which are determined from sets of frozen configurations of local protein environment partial charges that provide static external fields in which electronic structure calculations are performed to determine inner-sphere vibrational effects. The outer-sphere contributions, however, are modeled by supposing that intrachromophore motions are small in amplitude and that long-range environmental effects on the excitation energy fluctuations can be approximated by considering the different interactions between moving environmental partial charges and different partial charges on the chromophore that represent its charge distributions in the ground and excited states.

Here we apply the QM normal model approach outlined in Sections 3.2–4.1 to compute the short-range contribution $J_{\alpha}^{\text{vib}}(\omega)$; the long-range component, $J_{\alpha}^{\text{inter}}(\omega)$, is obtained from a classical trajectory correlation function calculation, as outlined in Section 4.2.

4.1. Intrachromophore Vibrational Contributions: Quantum Chemical ONIOM Calculations of $J_{\alpha}^{\text{vib}}(\omega)$

The approach employed here begins with a series of configurations generated from MD calculations that sample fluctuations on the approximate MM ground-state potential precisely like the configurations used in the correlation function calculations outlined above. Now, however, rather than using the time history of these configurations to compute the excitation energy fluctuation correlation function, we use it to provide a sampling of initial geometries from which to start energy optimizations to find important local minima on the consistent ground-state surface computed from quantum electronic structure calculations. These ground-state QM geometry optimizations are performed on the porphyrin head group of each bacteriochlorophyll in the static field of the MM partial charges of the local environment using a system–environment partitioning with the ONIOM computational method. In some cases (75, 124), explicit hydrogen bonding groups in the local protein environment can be considered as part of the QM region to explore the effects of different types of treatment of these interactions on computed excitation energies and spectral densities.

Following QM ground-state geometry optimization, normal mode analysis yields the individual chromophore intramolecular vibrational frequencies and normal modes that describe harmonic

fluctuations about the local minimum reference geometry for each chromophore. Making the same assumptions about the dependence of the ground- and excited-state QM surfaces on normal mode coordinates as in Equations 18 and 19, we readily find that the excitation energy is linear in these coordinates, as described in Equation 21.

From this expression, it is clear that by simply monitoring the slope of the excitation energy gap by varying each normal mode coordinate, we can extract the coordinate offset between the ground- and excited-state surfaces, $Q_{i\alpha}^e - Q_{i\alpha}^g$, along each normal mode direction; these values can be used in Equation 20 to compute the reorganization energy for each mode. Substituting these results into Equation 23 provides an estimate of the site-dependent spectral density of a given chromophore. The results reported below were computed using this approach; the excitation energies were computed using TDDFT calculations along the DFT ground-state normal modes, including the presence of the static field owing to the MM partial charges of the local environment using the ONIOM partitioning.

The approach developed here is, in fact, completely general, and any electronic structure (QM) method can be employed, depending on the required accuracy and available computational resources. We have chosen DFT/TDDFT as a matter of convenience for the intramolecular spectral densities reported here. Similarly, different QM/MM partitioning schemes (125, 126) can be readily incorporated into these computations.

4.2. Intermolecular Environmental Contributions: Classical Force Field Calculations of $J_{\alpha}^{\text{inter}}(\omega)$

An estimate of the intermolecular environmental contributions to the spectral density, $J_{\alpha}^{\text{inter}}(\omega)$, can be obtained using the excitation energy gap fluctuation correlation function formalism outlined in Section 3.3.

We first run an ensemble of constrained MD trajectories in which the porphyrin chromophore region of each chlorophyll moves as a rigid body and all other atoms in the surrounding protein environment are allowed to move under the influence of the full ground-state MM force field. In this way, we avoid double-counting the intramolecular chromophore vibrations that are already described by the QM normal mode treatment used to compute $J_{\alpha}^{\text{vib}}(\omega)$, as detailed in the previous section (80, 81). Now, because we have separated the interactions into short- and long-range contributions, we can replace the full quantum calculation of the long-range terms in the excitation energy fluctuations by a simple, accurate approximation (81) that assumes that the different interactions between the ground- and excited-state charge distributions of the chromophores, relevant for the computation of the long-range component of the excitation energy, can be represented by difference partial charges $\delta z_i^{\alpha} = (z_{e_i}^{\alpha} - z_{g_i}^{\alpha})$ at the various charge sites, i , of each chromophore, α . For simplicity, the model adapted here employs the same ground- and excited-state partial charges, z_{g_i} and z_{e_i} , for all chromophores, and the values used are obtained from ground-state gas-phase minimum energy geometry calculations. These charge distributions have been fitted to the point charge model as detailed in Reference 119. In these calculations, the charge difference distribution of the chromophores is thus assumed to be identical for each chromophore, and the unique excitation energy gap fluctuations of a given chromophore arise from fluctuations in its individual long-range partial charge solvation environment. Thus, the instantaneous excitation energy gap of chromophore α at time t is computed according to the expression

$$\delta \epsilon_{\alpha}^{\text{lr}}(t) = \frac{1}{4\pi\epsilon_0} \sum_i \sum_K \frac{\delta z_i^{\alpha} Z_K^{\alpha}}{|r_i^{\alpha}(t) - R_K^{\alpha}(t)|}, \quad (30)$$

where the sum on i extends over difference partial charge sites located at positions r_i^α for chromophore α , and the sum on K extends over the partial charges, Z_K^α , located at R_K^α in the environment of chromophore α .

5. APPLICATIONS

5.1. Benchmark Calculations for Model Nonadiabatic Problems using the Partial Linearized Density Matrix and Iterative Partial Linearized Density Matrix Approaches

In this section, we use numerical calculations to demonstrate both the accuracy and the limitations of the PLDM method. In particular, we compute EET dynamics with a widely used model for photosynthetic light harvesting systems.

As outlined in Section 3, the key physical quantities that govern the behavior of the simple system–bath models of these systems are the site energies, ϵ_α , and electronic couplings, $\Delta_{\alpha,\gamma}$, which determine the energy gaps between the quantum subsystem states; they also determine the frequencies of the environmental bath modes and the strengths of their couplings to the quantum subsystem, as reflected in the local spectral density, $J_\alpha(\omega)$, associated with each chromophore. Accurate treatment of the coupled electron–nuclear quantum dynamics of the relevant system–bath models is crucial to exploring these processes, as is the construction of realistic models of the underlying physical system.

Figure 1a presents numerical results for the EET rate associated with excitation transfer from a single donor chromophore to a single acceptor chromophore at $T = 300$ K, over a broad range of solvent reorganization energies, λ . The model uses an electronic coupling of $\Delta = 20$ cm^{−1}, with the excitation energy gap between the donor and acceptor states of $\epsilon = \epsilon_D - \epsilon_A = 100$ cm^{−1}. A simple Lorentzian truncated Ohmic (Debye spectral density form) $J_\alpha(\omega) = 2\lambda\omega\tau_c/(1 + \omega^2\tau_c^2)$ is used, with solvent reorganization energy $\lambda = 100$ cm^{−1} and solvent relaxation time $\tau_c = 100$ fs, assuming independent and identical baths for each chromophore. The EET rate is computed using the PLDM method and compared with FRET results, Redfield equation results, and numerically exact results obtained from the hierarchical equations of motion (HEOM) approach (46). Whereas the FRET and Redfield equation descriptions only agree with the exact results for certain reorganization energies, the PLDM results agree quantitatively over the entire range of λ .

Figure 1

Benchmark calculations of EET dynamics with PLDM and IPLDM approaches. (a) The EET rate k between single donor and acceptor chromophores at $T = 300$ K, as a function of reorganization energy λ . (b) Exciton population of site 1 at $T = 77$ K in a model Fenna–Matthews–Olson (FMO) complex as described in Reference 46. (c,d) Excitation populations for all seven sites at $T = 77$ K in the same model as in panel b. Arrows indicate the quantum thermal population. (e) EET dynamics at $T = 77$ K in a model FMO complex as described in Reference 137, which contains high-frequency vibrational modes in the spectral density adapted from Reference 69. (f) EET dynamics computed with IPLDM at $T = 300$ K in a three-state model system, with parameters for \hat{H}_s adapted from Reference 137 and the parameter for \hat{H}_{sb} adapted from experimental frequency and Huang–Rhys factors in Reference 120. In panel a, the Redfield and hierarchical equations of motion (HEOM) results were adapted from Reference 39; in panel b, the exact results, the linearized semiclassical initial value representation (LSC-IVR) results, and the Poisson bracket mapping equation (PBME) results were adapted from References 47, 60, and 52, respectively; and in panel e, the quasi-adiabatic path integral (QUAPI) results were adapted from Reference 137. Panel a was adapted from Reference 130 with permission. Panels b–d were adapted from References 77 and 130 with permission.

Note that a maximal transfer rate is obtained with changing λ ; this behavior has been previously discussed in terms of environment-assisted quantum transport (131–135).

In **Figure 1b–d**, we present the evolution of the excited-state site populations during EET dynamics in a seven-state model of the FMO bacterial light harvesting complex (46) at low temperature, $T = 77$ K. This model, as well as simple variations on its theme, has become the workhorse for exploring the generic behavior of photosynthetic chromophore antenna systems. A simple Debye spectral density is again used to describe the system–bath interaction, with relaxation time $\tau_c = 50$ fs and reorganization energy $\lambda = 35$ cm^{−1}, assuming independent and identical baths for each chromophore.

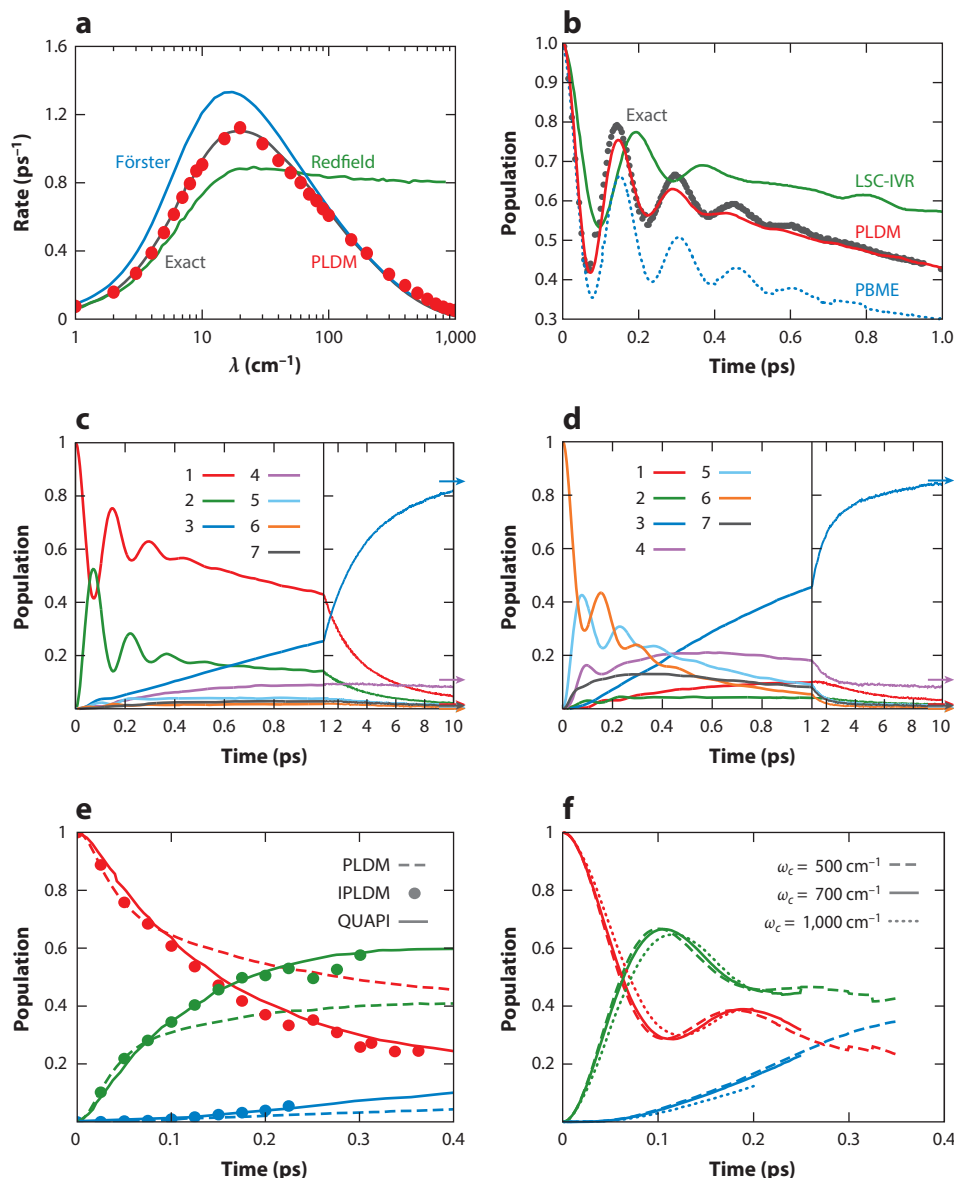


Figure 1b presents PLDM dynamics results for this model, again benchmarked against exact results obtained from HEOM calculations (46). The partially linearized dynamics scheme can reliably capture both short-time coherent EET dynamics and the long-time quantum thermal equilibrium distribution of the fully entangled system and bath (see **Figure 1c,d**) (77). Other approximate methods, such as the Ehrenfest mean-field approach (136) and fully linearized techniques including the LSC-IVR (52) and PBME (60) approaches, however, though successfully capturing the short-time coherent dynamics, fail to give the correct thermal equilibrium limit at long times. Comparing to the fully linearized approaches, more accurate results can be obtained by the partial linearized approach, for essentially the same numerical cost, because of the incorporation of both forward and backward dynamics for the evolution of the electronic DOFs.

The results displayed in **Figure 1c,d** explore the effects of starting in different initial electronic states of the quantum network and demonstrate that the PLDM approach reproduces the correct equilibration (as indicated with arrows) from different initial excitations.

Figure 1e shows the population dynamics at $T = 77$ K, computed using a recently developed model of EET in FMO (137). In this model, the spectral density is obtained using site energy fluctuation correlation functions computed with classical MD trajectories, as described in Equation 26 (the spectral density given by the gray curve in **Figure 5b** was used in these calculations). Compared to the numerically exact results provided here by quasi-adiabatic path integral (QUAPI) calculations (137), the result from PLDM calculations gives slower relaxation dynamics owing to the inaccurate, quasi-classical treatment of high-frequency vibrational modes that appear in this new model. This is a limitation of the PLDM method arising from the linearization approximation that is employed for the nuclear DOFs (79, 138). This results in a less accurate description of the dynamics of nuclear DOFs that exhibit strong quantum vibrational effects owing to high-frequency vibrational modes. However, when IPLDM is used (here with 1 hop/25 fs), the approach fully recovers the correct quantum dynamics, as indicated by the dots shown in **Figure 1e**. This encouraging result demonstrates how the results of PLDM calculations can be systematically improved by incorporating iterations of the short-time PLDM propagator, enabling the influence of quantum vibrational modes of the bath to be incorporated reliably.

Finally, **Figure 1f** presents the EET dynamics at $T = 300$ K for a reduced three-state FMO model. Here we study the dependence of the population dynamics obtained with converged IPLDM calculations as a function of truncating the spectral density by setting it to zero above various cutoff frequencies ω_c . Recent theoretical studies suggest that only those vibrational modes with frequencies comparable to the energy difference between the exciton states can significantly impact EET. Thus, if states are close in energy, the high-frequency quantum vibrational modes should have essentially no impact on the exciton dynamics (57, 137). Coupled high-frequency vibrations, however, artificially exchange energy with the quantum subsystem if treated with the linearized approximation, including when employing PLDM, because any amount of energy can exchange with a classically treated oscillator. This is why it is crucial that the IPLDM approach be employed to prevent this unphysical energy exchange to high-frequency modes. To verify this point, we truncate the spectral density at various cutoff values ω_c and use IPLDM to obtain accurate, converged EET dynamics results. The largest excitation energy difference in the \hat{H}_s is less than 500 cm^{-1} , and indeed, we find that if we include higher-frequency modes, their presence does not significantly impact the EET dynamics once the iterative scheme is converged. Although the higher-frequency vibrational modes, if treated reliably, should not promote excitation transfer, they do nonetheless add additional difficulty for converging our IPLDM calculations because of the pronounced nuclear quantum vibrational effects that must be represented. For example, the iteration rates to converge the IPLDM calculation for the $\omega_c = 500, 700$, and $1,000 \text{ cm}^{-1}$ cases

are, respectively, 1 hop/25 fs, 1 hop/10 fs, and 1 hop/1 fs, with significantly increased numerical demands for higher iteration rates.

In summary, numerical experience from the studies of EET problems across a broad range of parameter regimes has demonstrated that the partial linearized approach usually provides more accurate dynamics for electronic DOFs compared to dynamical mean-field or fully linearized approaches. This arises because of the more complete treatment of electronic interference that results when different forward and backward electronic mapping variable paths are incorporated explicitly in the algorithm. Similar findings have also been presented in studies of the forward-backward solution of the mixed quantum-classical Liouville equation (104, 105). However, when accuracy beyond the partial linearized approximation is required, for example for longer time propagation, or when nuclear quantum effects for the high-frequency vibrational modes play a role, one can always implement the IPLDM scheme to systematically improve the accuracy. As the number of iterations increases, accumulating the phase factors associated with short-time evolution to generate accurate off-diagonal elements of the propagator and iterating the result can come with more demanding numerical costs (79). The practical choice is, then, a balance between accuracy and numerical costs.

5.2. Intrachromophore Vibrational Components of Chromophore Spectral Densities in the Fenna–Matthews–Olson Complex

As detailed in Section 4, the approach we implement here allows us to decompose the system-bath interactions into short- and long-range contributions. In this section, we analyze short-range intrachromophore vibrational contributions to the local spectral densities computed according to the results given in Section 4.1 and compare them with experimental results and the contributions from the long-range intermolecular spectral density components considered above.

In **Figure 2**, we show an example of how these calculations are performed, which also demonstrates the reliability of the bilinearly coupled harmonic bath model used for these systems. As outlined in Section 4.1, configurations sampled from a long MD trajectory computed using the CHARMM simulation program provide a sampling of starting points for local DFT ground-state QM geometry optimizations, and TDDFT is employed to compute the excited-state energies; both calculations fully incorporate the static MM charges through the ONIOM QM/MM strategy. The range-separated Heyd–Scuseria–Ernzerhof (HSE) functional (140) is used, in which pure DFT semilocal exchange is used at long range and exact exchange is incorporated at short range, with a 0.25 contribution at $r = 0$ and a range separation parameter of $\omega = 0.11$. All calculations use the 6-31G(d) basis set.

Figure 2a shows highest occupied molecular orbitals and lowest unoccupied molecular orbitals from our QM/MM TDDFT calculation, between which the dominant transitions take place. **Figure 2b** plots the variation of the ground and excited electronic state energies as a function of a QM ground-state normal mode coordinate, here obtained by displacing along the coordinate of normal mode number 30 for each of the eight FMO monomer chromophores. Similar quality of the displaced harmonic model is observed for all modes in this system.

The relative coordinate displacement between ground and excited states determined by the slope of $\delta\epsilon_\alpha(\mathbf{Q}_\alpha)$ as defined in Equation 21 and presented in **Figure 2b** are generally less sensitive to the detailed choice of density functional compared to the site energies ϵ_α , which are often more reliably chosen to fit experiment. The reorganization energy and spectral density results obtained from these HSE calculations, for example, are very similar to those obtained from calculations employing the CAM-B3LYP functional (141) with an optimized range separation parameter, $\mu = 0.2$ (124). This relative insensitivity to choice of functional of our computed spectral density

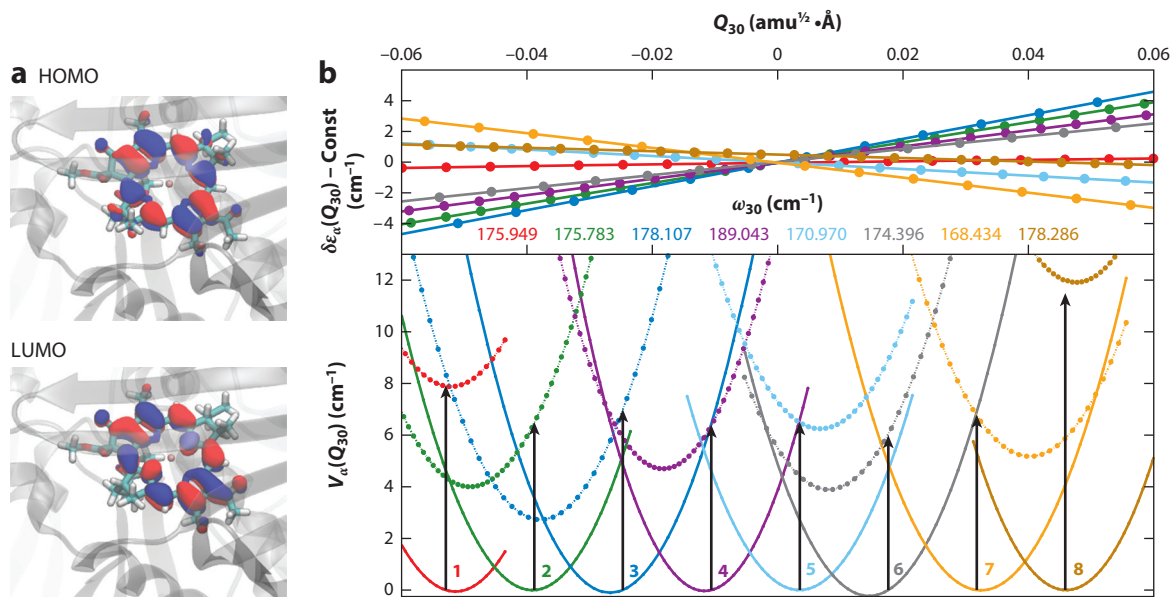


Figure 2

Time-dependent density functional theory (TDDFT) approach, using the ONIOM computational method, for computing intrachromophore spectral densities. (a) Highest occupied molecular orbital (HOMO) and lowest unoccupied molecular orbital (LUMO) obtained using TDDFT, between which the dominant transitions take place. (b, top) Linearity of difference between ground- and excited-state curves $\delta\epsilon_\alpha(Q_{i_\alpha})$ generated by normal mode displacement, as described in Equation 21. (b, bottom) Cuts through ground-state potential $V_\alpha^g(Q_{i_\alpha})$ and excited-state potentials $V_\alpha^e(Q_{i_\alpha})$ obtained by displacing along quantum ground-state normal mode number 30 for each chromophore with indicated frequencies ω_{30} . Arrows indicate Franck-Condon excitations.

results and the detailed comparison with experimental results presented in **Figure 3**, for example, suggest that the reorganization energies and spectral densities are often very reliably reproduced by these computational methods.

Figure 3 presents an overview of the low frequency dependence of the exciton-phonon coupling by comparing the experimental Huang-Rhys (HR) factors obtained from difference fluorescence line narrowing measurements (120) with those computed using Equations 20–22 for the different bacteriochlorophyll chromophores in the FMO light harvesting complex. **Figure 3** compares the experimental ΔFLN results with calculated HR factors for the different chromophores in their distorted local geometries and different local protein environments depicted in **Figure 3c**. We see that, although the calculations predict some variation from chromophore to chromophore in the HR factors, the general trends are all quite similar for the various chromophores and they match well with experimental results. In the ΔFLN experimental setup, the distinct absorption peak of BChl3 is selectively excited, so the experimental results should resemble the calculated BChl3 results more closely than any of the other chromophores. That said, the calculation results presented here do not include any configurational averaging. To model this effect, in **Figure 3b**, we present the spectral densities obtained by Gaussian broadening both the experimental and calculated results using a variance of $\sigma = 10 \text{ cm}^{-1}$. The low-amplitude dashed curves overlaid in each section of **Figure 3b** are the long-range intermolecular contributions to the spectral density computed for each chromophore, as detailed in Section 4.2, and can be found in Reference 80. Clearly, the intermolecular contributions to the spectral densities are generally substantially

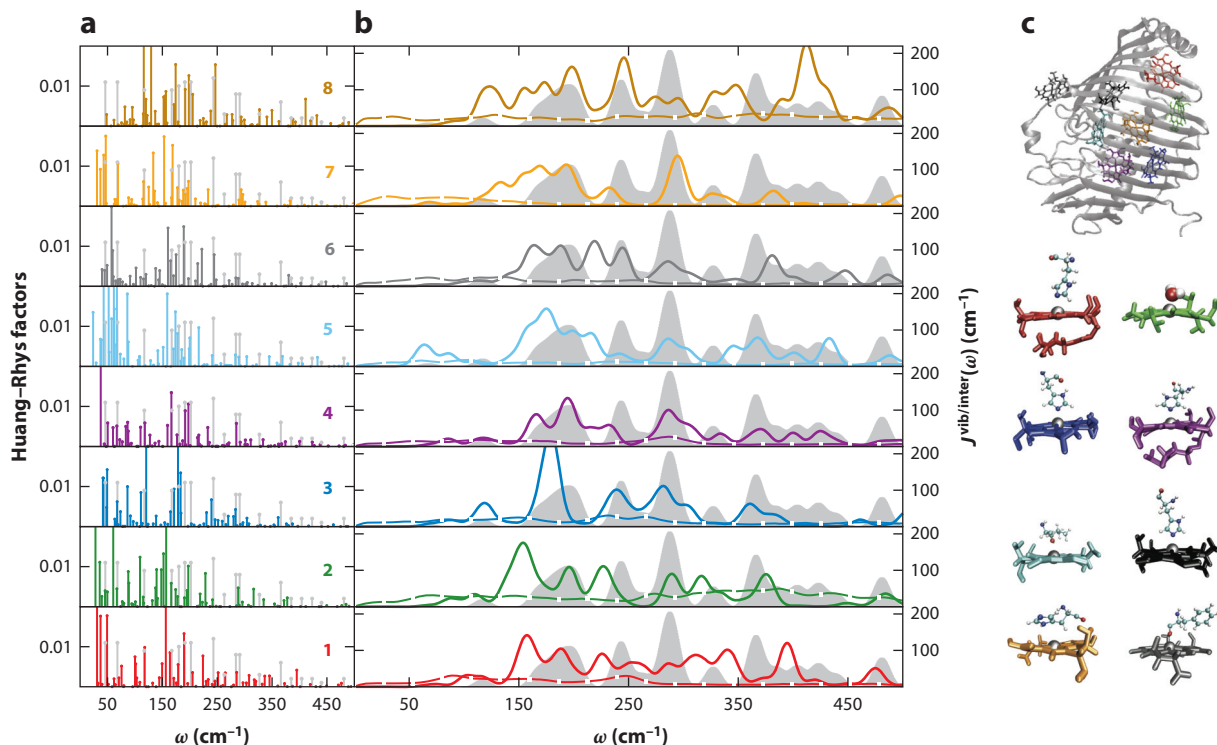


Figure 3

(a) Comparison of experimental Huang–Rhys (HR) factors (gray) with ONIOM quantum mechanical normal mode displacement calculations. (b) For chromophores numbered 1–8, shown are the low-frequency region of Gaussian broadened intramolecular spectral densities, $J^{\text{vib}}(\omega)$ (solid lines); long-range intermolecular spectral density contributions, $J^{\text{inter}}(\omega)$ (broken lines); and spectral densities obtained by broadening experimental HR factor results (gray regions) (120). (c) Typical snapshot configuration of each of the BCHs in an FMO monomer showing different local groups that coordinate the central magnesium of each porphyrin.

smaller than the short-range intramolecular contributions, although at the very lowest frequencies, the intermolecular spectral density dominates.

To quantify the differences between inter- and intramolecular spectral densities, we consider the various components of the reorganization energy. In contrast to the typical intermolecular reorganization energy of ~ 30 cm⁻¹, the computed intramolecular components are some four to six times larger, in the range ~ 120 – 180 cm⁻¹, and in good qualitative agreement with the experimental ΔFLN reorganization energy estimate of ~ 209 cm⁻¹. Because the intermolecular spectral density is generally much smaller than the intramolecular component, it only plays a role at low frequencies, where it dominates and is fairly structureless. The larger amplitude of the intramolecular spectral density, however, suggests that its more structured, higher-frequency dependence may play a role relaxing higher-energy nonradiative electronic transitions between chromophores.

Figure 4 shows the general agreement between the experimental spectral density (120, 121) and the spectral densities $J_{\alpha}(\omega)$ computed using the decomposition strategy $J_{\alpha}(\omega) = J_{\alpha}^{\text{vib}}(\omega) + J_{\alpha}^{\text{inter}}(\omega)$ across the entire frequency range. There are three clear bands of modes that span the frequency ranges ~ 0 – 700 cm⁻¹, ~ 700 – $1,200$ cm⁻¹, and $\sim 1,200$ – $1,800$ cm⁻¹, and each contributes about equally to the overall reorganization energy. We clearly see the three distinct bands of frequency

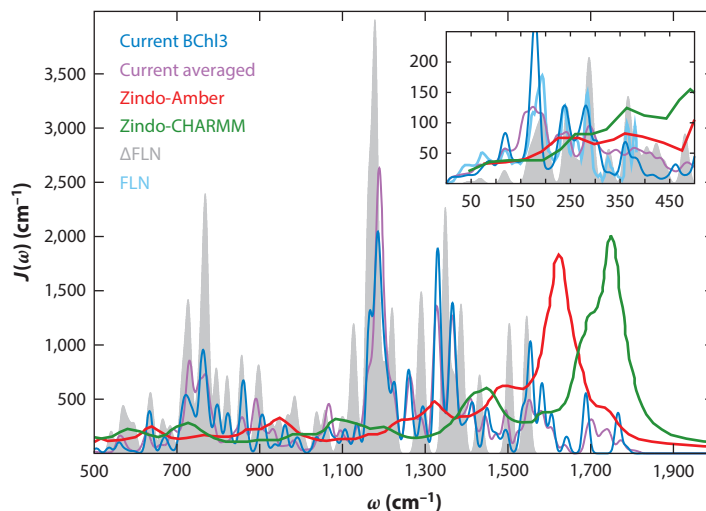


Figure 4

Comparison of the spectral density in the Fenna–Matthews–Olson (FMO) photosynthetic light harvesting complex, including the current decomposing approach, $J_{\alpha}(\omega) = J_{\alpha}^{\text{vib}}(\omega) + J_{\alpha}^{\text{inter}}(\omega)$, for BChl3 (blue lines) and for an average over chromophores (purple lines) as well as results from molecular dynamics correlation function calculations with different molecular mechanics force fields, ZINDO-Amber (red lines) and ZINDO-CHARMM (green lines). Gaussian broadened intramolecular spectral densities extracted from difference fluorescence line narrowing (Δ FLN) experiments are shown as well (gray regions) (120). (Inset) Low-frequency behavior in detail; low-frequency fluorescence line narrowing (FLN) experimental data (121) are presented (cyan lines). ZINDO-Amber and ZINDO-CHARMM results are adapted from References 75 and 76.

response reproduced in both experiment and theory. The insert in **Figure 4** analyzes the low-frequency band, and the main panel explores the high-frequency bands. Overlaid in the figure are the results of recent MD correlation function calculations of the FMO spectral density obtained using different force fields (75, 76) and applying the ZINDO/CIS approach to compute the excitation energies along the trajectories, as outlined in Section 3.3. These MD correlation function results are averaged over the different chromophores. From the insert, we see that the low-frequency envelope of the spectral density is captured reasonably well by the Amber force field correlation function calculations, whereas the CHARMM results somewhat overestimate the amplitude of the spectral density in this region. In the main panel of **Figure 4**, however, we see that the most significant differences between the MD correlation function spectral densities and the experimental results is the failure to reliably capture the three-band structure; in particular, it misses the large-amplitude mid-range frequency response and gives large, unphysical amplitudes to the highest-frequency modes.

Recent computational studies (75) suggest that the discrepancies between the ZINDO-MM spectral density and the experimental spectral density, at least at low frequency, is due in part to the inaccuracy of the ZINDO method itself. When TDDFT-MM is employed, however, low-frequency spectral density results that more closely match with experiment can be obtained (75), although this can be sensitive to choice of functional and MM force field (75). Nevertheless, all these MM correlation function–based approaches still generate residual discrepancies at higher frequencies that cannot be explained purely by the inaccuracy of the electronic structure method.

A recent theoretical analysis (124) points the way to understanding this problem. The MM potentials that govern the correlation function–based method may in general have different

frequencies, $\Omega_{i\alpha}$, and different normal modes, \mathbf{q}_α , from those of the ground- and excited-state surfaces obtained from the electronic structure calculations as approximated, for example, by Equations 18 and 19. Further, the equilibrium position of the MM surface, $\{q_{i\alpha}^{\text{MM}}\}$, is in general also different, so for the sake of analysis we can write the MM surface as

$$V_\alpha^{\text{MM}}(\mathbf{q}_\alpha) = \frac{1}{2} \sum_{i\alpha} \Omega_{i\alpha}^2 (q_{i\alpha} - q_{i\alpha}^{\text{MM}})^2 + E_\alpha^{\text{MM}}, \quad (31)$$

and the rotation between the MM and QM normal modes is determined by the transformation matrix elements $D_{k\alpha i\alpha} = \hat{\mathbf{q}}_{i\alpha}^T \hat{\mathbf{Q}}_{k\alpha}$, where the $\hat{}$ symbols indicate unit vectors in the $(3N - 6)$ -dimensional Cartesian space describing chromophore α 's vibrations. A simple calculation of the QM excitation energy gap correlation function using trajectories evolving over this harmonic approximation to the MM surface reveals that the spectral density computed with the MM correlation function approach actually has the form

$$J_\alpha^{\text{MM}}(\omega) = \pi \omega \sum_{i\alpha} \sum_{k\alpha} \left(\frac{\omega_{k\alpha} D_{k\alpha i\alpha}}{\Omega_{i\alpha}} \right)^2 \lambda_{k\alpha} \delta(\omega - \Omega_{i\alpha}). \quad (32)$$

From this result it is clear that the MD correlation function estimate of the spectral density has peaks at the MM frequencies rather than at the frequencies corresponding to the actual electronic structure potential surface, as with the true spectral density given by Equation 23. Further, the amplitudes of these peaks, in general, involve linear combinations of the actual electronic structure-determined reorganization energies with the combination coefficients being governed by the transformation between the MM surface and the QM surface normal modes and the ratio of the frequencies of these modes. Qualitatively, the effect of these linear combinations is to smear out the peaks in the true spectral density by adding different amounts of the various electronic structure-determined reorganization energies with coefficients $(\omega_{k\alpha} D_{k\alpha i\alpha} / \Omega_{i\alpha})^2$, as described in Equation 32, rather than having pure peaks associated with each individual mode at its true frequency, as in Equation 23. This Duschinsky-like linear combination effect is expected to contribute significantly to suppressing the amplitudes of the true spectral density peaks when the spectral density is approximated using the MD correlation function approach. Further, model studies of BChl molecules (124) employing the same level of QM theory and the same MM surfaces as widely used in correlation function calculations (75) suggest that at higher frequencies, the QM and MM normal mode frequencies can deviate significantly from each other, with the MM surface overestimating the intrachromophore vibrational frequencies by as much as a few hundred wavenumbers. These effects contribute to the significant deviations of the spectral densities computed with the ZINDO-CHARMM and ZINDO-Amber correlation function approaches detailed in **Figure 4**.

5.3. Excitation Energy Transfer Dynamics in the Fenna–Matthews–Olson Complex

In **Figure 5**, we explore the influence of the different components of the spectral density on the relaxation dynamics of a reduced five-state FMO model that includes BChls 1, 2, 3, 4, and 8 with system Hamiltonian parameters from Reference 50. Results are presented for $T = 77$ K and $T = 300$ K.

Figure 5a shows the site population dynamics for the system–bath Hamiltonian that includes only our computed site-dependent intermolecular spectral density (solid curves), as well as for a model Hamiltonian with the full (computed inter- + intramolecular) site-dependent spectral density. In each case, BChl1 is initially excited, and the bath modes are initialized in their independent thermal equilibrium states. The large differences between the population dynamics for

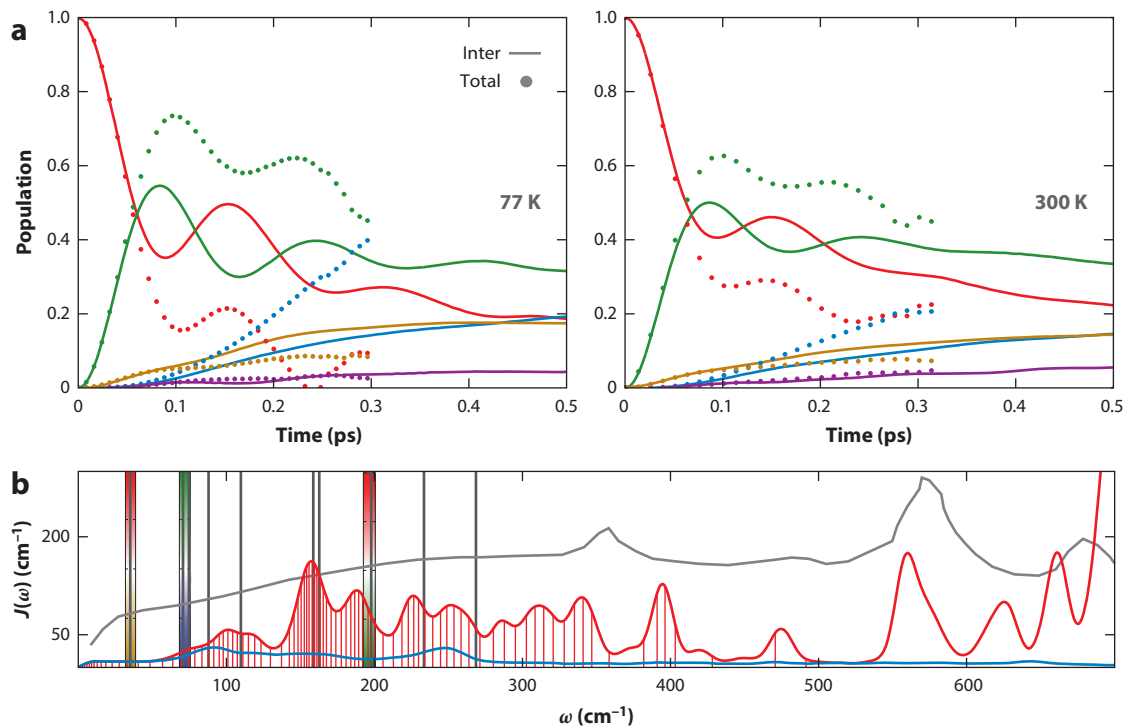


Figure 5

Excitation transfer dynamics in a model of the Fenna–Matthews–Olson (FMO) complex with realistic spectral density. (a) Site basis state population dynamics obtained with an iterated partial linearized density matrix approach for an intermolecular-only spectral density model (solid curves) and for an inter + intramolecular spectral density model (dots) at $T = 77$ K and $T = 300$ K. The sites are BChl1 (red), BChl2 (green), BChl3 (blue), BChl4 (purple), and BChl8 (brown). (b) Total spectral density (red curve) is compared with intermolecular spectral density (blue curve) for BChl1 in the FMO complex; densities are computed using the methods of Section 4 and are the same as the BChl1 densities in **Figure 3**. Vertical red lines under the red curve show individual bath oscillator frequencies used in spectral density discretization. MM-ZINDO/CIS correlation function spectral density (69) (gray curve) is also shown for comparison. Dark gray vertical lines and two-color vertical bars show energy differences between quantum subsystem eigenstate (exciton) energies; specifically, two-color bars show energy differences between exciton states dominated by specific example site basis states: red-green (1, 2), green-blue (2, 3), red-brown (1–8).

these models suggest that both the inter- and intramolecular components of our realistic spectral density play significant roles in the electronic relaxation and EET in this model system.

When only the broad, low-amplitude, low-frequency intermolecular component is present, the coupled system–bath dynamics (**Figure 5a**) rapidly produces a linear combination of the strongly coupled ($\Delta_{12} = -80.3 \text{ cm}^{-1}$) BChl1 and BChl2 site basis states with essentially equal components of higher-energy ($\epsilon_1 = 185.4 \text{ cm}^{-1}$) and lower-energy ($\epsilon_2 = 80.6 \text{ cm}^{-1}$) sites. The result of this early time-coupled system–bath dynamics is thus an entangled state (143) in which much of the energy still resides in the chromophore electronic subsystem, with little energy transferred to the bath because of the weaker, intermolecular-only system–bath coupling. In fact, the site basis populations show underdamped coherent oscillatory features in this weak system–bath coupling entangled state.

In **Figure 5b**, we show the relevant spectral densities overlaid with vertical lines at the transition energies between the system Hamiltonian eigenstates (excitonic states) (30, 33). The graded vertical color bars show the excitonic energy differences between eigenstates that are

predominately composed of a given site basis state. Thus, for example, the red and green bar at $\sim 200\text{ cm}^{-1}$ corresponds to the energy difference between eigenstates that are dominated by site basis states BChl1 and BChl2, respectively; the green and blue bar highlights the transition energy between eigenstates dominated by BChl2 and BChl3; etc. The relatively low magnitude of the intermolecular spectral density at 200 cm^{-1} is responsible for the early-time intermolecular-only system–bath dynamics.

When the full spectral density is employed, however, we see that the early-time relaxation results (dots in **Figure 5a**) in a new superposition state of sites 1 and 2 has a much higher population of the low-energy BChl2 state compared to the very small population of the BChl1 state. In this composite system–bath entangled state, much of the initial excitation energy has thus been transferred to the bath as a result of the strong system–bath coupling arising from the substantial intramolecular component in the full spectral density at 200 cm^{-1} (red and green bar in **Figure 5b**). Once the BChl2 state dominates the population, we see a rapid increase in the BChl3 state population because of the BChl2–BChl3 site coupling in the system Hamiltonian. In fact, this is the only active path to populating the BChl3 state in this model (32, 80, 144–147). The excitonic energy gap between eigenstates dominated by BChl2 and BChl3 occurs at about 70 cm^{-1} (green and blue bar in **Figure 5b**), where the spectral density is dominated by intermolecular contributions. Thus, these calculations suggest that, depending on the energy difference between the exciton states involved in the transition, different parts of the bath can be responsible for the relaxation.

Because the role of the FMO complex is to funnel energy to the lowest-energy BChl3 site (3, 46, 147), the coupling to the intramolecular bath modes plays an important role in accelerating EET to BChl3 in this model. From **Figure 5a**, we see that significantly slower buildup of BChl3 population occurs when only the weak intermolecular bath coupling is present.

The ZINDO-CHARMM spectral density (75, 76) also displayed in **Figure 5b** significantly overestimates the low-frequency spectral density compared to the inter- + intramolecular spectral density calculated here. The benchmark dynamics results presented in **Figure 1e** use this strong spectral density and give qualitatively different population dynamics that is completely overdamped and that shows much slower energy transfer (137, 142) and no evidence of coherent population dynamics, which is inconsistent with the findings of two-dimensional coherent spectroscopy experiments (3, 4).

Determining the relative magnitudes of the inter- and intramolecular components of the spectral density is crucial to obtaining realistic EET dynamics. This requires careful implementation of accurate computational methods that may challenge existing MM force field approaches, and the approach we outlined in this review opens up many possibilities for further developing more accurate yet efficient techniques.

6. CONCLUDING REMARKS AND OUTLOOK

In this review, rather than presenting a broad overview of many different computational methods for treating EET in complex material and biological systems, we have instead focused on a selected set of methods for which we have tried to give a complete and detailed overview. These include general techniques for propagating the dynamics of complex electronically excited systems in the presence of dissipative environments as well as methods for developing highly accurate system–bath models for such systems that can be efficiently treated by these dynamics methods.

The linearized dynamics methods we have presented can be reliable for systems in which the environmental DOFs can be approximated quasi-classically, e.g., systems with low-frequency vibrational motions. We have shown that the approach can be systematically improved to treat higher-frequency quantum environmental modes, but this can come at a significant computational

cost. Nevertheless, the dynamical methods detailed here can be generally applied, and they scale comparably to other available techniques.

The method we have introduced for constructing reliable model system–bath interaction Hamiltonians from first principles avoids many of the problems that are highlighted here, which plague other widely used MD correlation function approaches based on parameterized one-size-fits-all MM force fields. We show how to compute these model Hamiltonians without calculating correlation functions, which can require large numbers of expensive excited-state quantum electronic structure calculations, and which even then can result in erroneous descriptions of the system–bath coupling because of an inadequate underlying MM force field governing the time correlation function dynamics.

Despite that the methods developed here can, in principle, be applied generally, our application focus in this review has been on EET in photosynthetic light harvesting. A topic of great current interest in this area is the question of the importance of different types of coherent quantum dynamics in these complex biological systems, e.g., electronic versus vibrational or vibronic. These questions are very difficult to answer unequivocally with currently available experimental techniques, but the toolbox of computational methods that we have reviewed offers great promise for approaching these important open questions from basic theoretical principles.

DISCLOSURE STATEMENT

The authors are not aware of any affiliations, memberships, funding, or financial holdings that might be perceived as affecting the objectivity of this review.

ACKNOWLEDGMENTS

We gratefully acknowledge support for this research from the National Science Foundation under grants CHE-0911635 and CHE-1301157 and support from Science Foundation Ireland under grant 10/IN.1/I3033. We are extremely grateful to Sara Bonella and William Miller for their insights throughout the development of the linearized dynamics methods, and we are grateful to Eva Rivera, Daniel Montemayor, and Marco Masia for their valuable contributions to the development of spectral density computation methods; Emily Dunkel for her contribution to the development of the original iteration scheme; and Tom Miller for his contribution to the development of the rate constant calculation with PLDM.

LITERATURE CITED

1. Blankenship RE. 2014. *Molecular Mechanisms of Photosynthesis*. Chichester, UK: Blackwell
2. Chenu A, Scholes GD. 2015. Coherence in energy transfer and photosynthesis. *Annu. Rev. Phys. Chem.* 66:69–96
3. Engel GS, Calhoun TR, Read EL, Ahn T-K, Mancal T, et al. 2007. Evidence for wavelike energy transfer through quantum coherence in photosynthetic systems. *Nature* 446:782–86
4. Panitchayangkoon G, Hayes D, Fransted KA, Caram JR, Harel E, et al. 2010. Long-lived quantum coherence in photosynthetic complexes at physiological temperature. *PNAS* 107:12766–70
5. Panitchayangkoon G, Voronine DV, Abramavicius D, Caram JR, Lewis NHC, et al. 2011. Direct evidence of quantum transport in photosynthetic light-harvesting complexes. *PNAS* 108:20908–12
6. Collini E, Wong CY, Wilk KE, Curmi PMG, Brumer P, Scholes GD. 2010. Coherently wired light-harvesting in photosynthetic marine algae at ambient temperature. *Nature* 463:644–47

7. Abramavicius D, Palmieri B, Voronine D, Sanda F, Mukamel S. 2009. Coherent multidimensional optical spectroscopy of excitons in molecular aggregates; quasiparticle versus supermolecule perspectives. *Chem. Rev.* 109:2350–408
8. Mukamel S, Abramavicius D, Yang L, Zhuang W, Schweigert IV, Voronine DV. 2009. Coherent multi-dimensional optical probes for electron correlations and exciton dynamics: from NMR to X-rays. *Acc. Chem. Res.* 42:553–62
9. Wong CY, Alvey RM, Turner DB, Wilk KE, Bryant DA, et al. 2012. Electronic coherence lineshapes reveal hidden excitonic correlations in photosynthetic light harvesting. *Nat. Chem.* 4:396–404
10. Schlau-Cohen GS, Calhoun TR, Ginsberg NS, Ballottari M, Bassi R, Fleming GR. 2012. Spectroscopic elucidation of uncoupled transition energies in the major photosynthetic light-harvesting complex, LHCII. *PNAS* 107:13276–81
11. Schlau-Cohen GS, Calhoun TR, Ginsberg NS, Read EL, Ballottari M, et al. 2009. Pathways of energy flow in LHCII from two-dimensional electronic spectroscopy. *J. Phys. Chem. B* 113:15352–63
12. Schlau-Cohen GS, Ishizaki A, Calhoun TR, Ginsberg NS, Ballottari M, et al. 2012. Elucidation of the timescales and origins of quantum electronic coherence in LHCII. *Nat. Chem.* 4:389–95
13. Harel E, Engel GS. 2012. Quantum coherence spectroscopy reveals complex dynamics in bacterial light-harvesting complex 2 (LH2). *PNAS* 109:706–11
14. Fidler AF, Singh VP, Long PD, Dahlberg PD, Engel GS. 2013. Time scales of coherent dynamics in the light-harvesting complex 2 (LH2) of *Rhodobacter sphaeroides*. *J. Phys. Chem. Lett.* 4:1404–9
15. Fidler AF, Singh VP, Long PD, Dahlberg PD, Engel GS. 2014. Dynamic localization of electronic excitation in photosynthetic complexes revealed with chiral two-dimensional spectroscopy. *Nat. Comm.* 5:3286
16. Romero E, Augulis R, Novoderezhkin VI, Ferretti M, Thieme J, et al. 2014. Quantum coherence in photosynthesis for efficient solar-energy conversion. *Nat. Phys.* 10:676–82
17. Hayes D, Wen J, Panitchayangkoon G, Blankenship RE, Engel GS. 2011. Robustness of electronic coherence in the Fenna–Matthews–Olson complex to vibronic and structural modifications. *Faraday Discuss.* 150:459–69
18. Turner DB, Dinshaw R, Lee K-K, Belsley MS, Wilk KE, et al. 2012. Quantitative investigations of quantum coherence for a light-harvesting protein at conditions simulating photosynthesis. *Phys. Chem. Chem. Phys.* 14:4857–74
19. Sarovar M, Ishizaki A, Fleming GR, Whaley KB. 2010. Quantum entanglement in photosynthetic light-harvesting complexes. *Nat. Phys.* 6:462–67
20. Abramavicius D, Mukamel S. 2010. Quantum oscillatory exciton migration in photosynthetic reaction centers. *J. Chem. Phys.* 133:064510
21. Abramavicius D, Mukamel S. 2010. Energy-transfer and charge-separation pathways in the reaction center of photosystem II revealed by coherent two-dimensional optical spectroscopy. *J. Chem. Phys.* 133:184501
22. Pachón LA, Brumer P. 2011. Physical basis for long-lived electronic coherence in photosynthetic light-harvesting systems. *J. Phys. Chem. Lett.* 2:2728–32
23. Tiwari V, Peters WK, Jonas DM. 2013. Electronic resonance with anticorrelated pigment vibrations drives photosynthetic energy transfer outside the adiabatic framework. *PNAS* 110:1203–8
24. Christensson N, Kauffmann HF, Pullerits T, Mancal T. 2012. Origin of long-lived coherences in light-harvesting complexes. *J. Phys. Chem. B* 116:7449–54
25. Plenio MB, Almeida J, Huelga SF. 2013. Origin of long-lived oscillations in 2D-spectra of a quantum vibronic model: electronic versus vibrational coherence. *J. Chem. Phys.* 139:235102
26. Chin AW, Prior J, Rosenbach R, Caycedo-Soler F, Huelga SF, Plenio MB. 2013. The role of non-equilibrium vibrational structures in electronic coherence and recoherence in pigment–protein complexes. *Nat. Phys.* 9:113–18
27. Mohseni M, Omar Y, Engel GS, Plenio MB. 2014. *Quantum Effects in Biology*. Cambridge, UK: Cambridge Univ. Press
28. Scholes GD. 2010. Quantum-coherent electronic energy transfer: Did nature think of it first? *J. Phys. Chem. Lett.* 1:2–8

29. Scholes GD, Fleming GR, Olaya-Castro A, van Grondelle R. 2012. Lessons from nature about solar light harvesting. *Nat. Chem.* 3:763–74
30. Strümpfer J, Şener M, Schulten K. 2012. How quantum coherence assists photosynthetic light-harvesting. *J. Phys. Chem. Lett.* 3:536–42
31. Huo P, Coker DF. 2011. Theoretical study of coherent excitation energy transfer in cryptophyte phycoerythrin 645 at physiological temperature. *J. Phys. Chem. Lett.* 2:825–33
32. Moix J, Wu J, Huo P, Coker DF, Cao J. 2011. Efficient energy transfer in light-harvesting systems, III: the influence of the eighth bacteriochlorophyll on the dynamics and efficiency in FMO. *J. Phys. Chem. Lett.* 2:3045–52
33. Fassioi F, Dinshaw R, Arpin PC, Scholes GD. 2013. Photosynthetic light harvesting: excitons and coherence. *J. R. Soc. Interface* 11:20130901
34. Pachón LA, Brumer P. 2012. Computational methodologies and physical insights into electronic energy transfer in photosynthetic light-harvesting complexes. *Phys. Chem. Chem. Phys.* 14:10094–108
35. Jang S, Newton MD, Silbey RJ. 2004. Multichromophoric Förster resonance energy transfer. *Phys. Rev. Lett.* 92:218301
36. Heijs DJ, Malyshev VA, Knoester J. 2005. Decoherence of excitons in multichromophore systems: thermal line broadening and destruction of superradiant emission. *Phys. Rev. Lett.* 95:177402
37. Jang S, Newton MD, Silbey RJ. 2007. Multichromophoric Förster resonance energy transfer from B800 to B850 in the light harvesting complex 2: evidence for subtle energetic optimization by purple bacteria. *J. Phys. Chem. B* 111:6807–14
38. Ishizaki A, Fleming GR. 2009. On the adequacy of the Redfield equation and related approaches to the study of quantum dynamics in electronic energy transfer. *J. Chem. Phys.* 130:234110
39. Ishizaki A, Fleming GR. 2009. Unified treatment of quantum coherent and incoherent hopping dynamics in electronic energy transfer: reduced hierarchy equation approach. *J. Chem. Phys.* 130:234111
40. Palmieri B, Abramavicius D, Mukamel S. 2009. Lindblad equations for strongly coupled populations and coherences in photosynthetic complexes. *J. Chem. Phys.* 130:204512
41. Rebentrost P, Chakraborty R, Aspuru-Guzik A. 2009. Non-Markovian quantum jumps in excitonic energy transfer. *J. Chem. Phys.* 131:184102
42. Berkelbach TC, Markland TE, Reichman DR. 2012. Reduced density matrix hybrid approach: application to electronic energy transfer. *J. Chem. Phys.* 136:084104
43. Berkelbach TC, Reichman DR, Markland TE. 2012. Reduced density matrix hybrid approach: an efficient and accurate method for adiabatic and non-adiabatic quantum dynamics. *J. Chem. Phys.* 136:034113
44. Ishizaki A, Tanimura Y. 2005. Quantum dynamics of system strongly coupled to low-temperature colored noise bath: reduced hierarchy equations approach. *J. Phys. Soc. Jpn.* 74:3131–34
45. Shi Q, Chen LP, Nan GJ, Xu RX, Yan YJ. 2009. Efficient hierarchical Liouville space propagator to quantum dissipative dynamics. *J. Chem. Phys.* 130:084105
46. Ishizaki A, Fleming GR. 2009. Theoretical examination of quantum coherence in a photosynthetic system at physiological temperature. *PNAS* 106:17255–60
47. Zhu J, Kais S, Rebentrost P, Aspuru-Guzik A. 2011. Modified scaled hierarchical equation of motion approach for the study of quantum coherence in photosynthetic complexes. *J. Phys. Chem. B* 115:1531–37
48. Makri N, Makarov DE. 1995. Tensor propagator for iterative quantum time evolution of reduced density matrices. I. Theory. *J. Chem. Phys.* 102:4600–10
49. Makri N, Makarov DE. 1995. Tensor propagator for iterative quantum time evolution of reduced density matrices. II. Numerical methodology. *J. Chem. Phys.* 102:4611–18
50. Nalbach P, Braun D, Thorwart M. 2011. Exciton transfer dynamics and quantumness of energy transfer in the Fenna–Matthews–Olson complex. *Phys. Rev. E* 84:041926
51. Nalbach P, Ishizaki A, Fleming GR, Thorwart M. 2011. Iterative path-integral algorithm versus cumulant time-nonlocal master equation approach for dissipative biomolecular exciton transport. *New J. Phys.* 13:063040
52. Tao G, Miller WH. 2010. Semiclassical description of electronic excitation population transfer in a model photosynthetic system. *J. Phys. Chem. Lett.* 1:891–94
53. Kim HW, Kelly A, Park JW, Rhee YM. 2012. All-atom semiclassical dynamics study of quantum coherence in photosynthetic Fenna–Matthews–Olson complex. *J. Am. Chem. Soc.* 134:11640–51

54. Jang S, Cheng Y-C, Reichman DR, Eaves JD. 2008. Theory of coherent resonance energy transfer. *J. Chem. Phys.* 129:101104
55. Jang S. 2009. Theory of coherent resonance energy transfer for coherent initial condition. *J. Chem. Phys.* 131:164101
56. Jang S. 2011. Theory of multichromophoric coherent resonance energy transfer: a polaronic quantum master equation approach. *J. Chem. Phys.* 135:034105
57. Kolli A, O'Reilly E, Scholes GD, Olaya-Castro A. 2012. The fundamental role of quantized vibrations in coherent light harvesting by cryptophyte algae. *J. Chem. Phys.* 137:174109
58. Strümpfer J, Schulten K. 2012. Open quantum dynamics calculations with the hierarchy equations of motion on parallel computers. *J. Chem. Theory Comput.* 8:2808–16
59. Kreisbeck C, Kramer T, Aspuru-Guzik A. 2014. Scalable high-performance algorithm for the simulation of exciton dynamics. Application to the light-harvesting complex II in the presence of resonant vibrational modes. *J. Chem. Theory Comput.* 10:4045–54
60. Kelly A, Rhee YM. 2011. Mixed quantum–classical description of excitation energy transfer in a model Fenna–Matthews–Olsen complex. *J. Phys. Chem. Lett.* 2:808–12
61. Kim HW, Lee W-G, Rhee YM. 2014. Improving long time behavior of Poisson bracket mapping equation: a mapping variable scaling approach. *J. Chem. Phys.* 141:124107
62. Kim HW, Rhee YM. 2014. Improving long time behavior of Poisson bracket mapping equation: a non-Hamiltonian approach. *J. Chem. Phys.* 140:184106
63. Jurinovich S, Viani L, Curutchet C, Mennucci B. 2015. Limits and potentials of quantum chemical methods in modelling photosynthetic antennae. *Phys. Chem. Chem. Phys.* 17:30783–92
64. Sisto A, Glowacki DR, Martinez TJ. 2014. Ab initio nonadiabatic dynamics of multichromophore complexes: a scalable graphical-processing-unit-accelerated exciton framework. *Acc. Chem. Res.* 47:2857–66
65. Olbrich C, Kleinekathfer U. 2010. Time-dependent atomistic view on the electronic relaxation in light-harvesting system II. *J. Phys. Chem. B* 114:12427–37
66. Olbrich C, Strümpfer J, Schulten K, Kleinekathfer U. 2011. Quest for spatially correlated fluctuations in the FMO light-harvesting complex. *J. Phys. Chem. B* 115:758–64
67. Shim S, Rebentrost P, Valleau S, Aspuru-Guzik A. 2012. Atomistic study of the long-lived quantum coherences in the Fenna–Matthews–Olson complex. *Biophys. J.* 102:649–60
68. Damjanovic A, Kosztin I, Kleinekathfer U, Schulten K. 2002. Excitons in a photosynthetic light-harvesting system: a combined molecular dynamics, quantum chemistry, and polaron model study. *Phys. Rev. E* 65:031919
69. Olbrich C, Strümpfer J, Schulten K, Kleinekathfer U. 2011. Theory and simulation of the environmental effects on FMO electronic transitions. *J. Phys. Chem. Lett.* 2:1771–76
70. Valleau S, Eisfeld A, Aspuru-Guzik A. 2012. On the alternatives for bath correlators and spectral densities from mixed quantum–classical simulations. *J. Chem. Phys.* 137:224103
71. Aghtar M, Strümpfer J, Olbrich C, Schulten K, Kleinekathfer U. 2014. Different types of vibrations interacting with electronic excitations in phycoerythrin 545 and Fenna–Matthews–Olson antenna systems. *J. Phys. Chem. Lett.* 5:3131–37
72. Viani L, Corbella M, Curutchet C, O'Reilly EJ, Olaya-Castro A, Mennucci B. 2014. Molecular basis of the exciton–phonon interactions in the PE545 light-harvesting complex. *Phys. Chem. Chem. Phys.* 16:16302–11
73. Kim CW, Park JW, Rhee YM. 2015. Effect of chromophore potential model on the description of exciton–phonon interactions. *J. Phys. Chem. Lett.* 6:2875–80
74. Renger T, Klinger A, Steinecker F, Schmidt am Busch M, Numata J, Müh F. 2012. Normal mode analysis of the spectral density of the Fenna–Matthews–Olson light-harvesting protein: how the protein dissipates the excess energy of excitons. *J. Phys. Chem. B* 116:14565–80
75. Chandrasekaran S, Aghtar M, Valleau S, Aspuru-Guzik A, Kleinekathfer U. 2015. Influence of force fields and quantum chemistry approach on spectral densities of BChl *a* in solution and in FMO proteins. *J. Phys. Chem. B* 119:9995–10004
76. Wang X, Ritschel G, Wuster S, Eisfeld A. 2015. Open quantum system parameters for light harvesting complexes from molecular dynamics. *Phys. Chem. Chem. Phys.* 17:25629–41

77. Huo P, Coker DF. 2011. Partial linearized density matrix dynamics for dissipative, non-adiabatic quantum evolution. *J. Chem. Phys.* 135:201101
78. Huo P, Coker DF. 2012. Semi-classical path integral non-adiabatic dynamics: a partial linearized classical mapping Hamiltonian approach. *Mol. Phys.* 110:1035–52
79. Huo P, Coker DF. 2012. Consistent schemes for non-adiabatic dynamics derived from partial linearized density matrix propagation. *J. Chem. Phys.* 137:22A535
80. Rivera E, Montemayor D, Masia M, Coker DF. 2013. Influence of site-dependent pigment–protein interactions on excitation energy transfer in photosynthetic light harvesting. *J. Phys. Chem. B* 117:5510–21
81. Jing Y, Zheng R, Li H-X, Shi Q. 2012. Theoretical study of the electronic–vibrational coupling in the Q_y states of the photosynthetic reaction center in purple bacteria. *J. Phys. Chem. B* 116:1164–71
82. Adolphs J, Renger T. 2006. How proteins trigger excitation energy transfer in the FMO complex of green sulfur bacteria. *Biophys. J.* 91:2778–97
83. Miller WH. 2001. The semiclassical initial value representation: a potentially practical way for adding quantum effects to classical molecular dynamics simulations. *J. Phys. Chem. A* 105:2942–55
84. Miller WH. 2012. Quantum or classical coherence? *J. Chem. Phys.* 136:210901
85. Sun X, Wang H, Miller WH. 1998. Semiclassical theory of electronically nonadiabatic dynamics: results of a linearized approximation to the initial value representation. *J. Chem. Phys.* 109:7064–74
86. Kelly A, van Zon R, Schofield J, Kapral R. 2012. Mapping quantum–classical Liouville equation: projectors and trajectories. *J. Chem. Phys.* 136:084101
87. Kim H, Nassimi A, Kapral R. 2008. Quantum–classical Liouville dynamics in the mapping basis. *J. Chem. Phys.* 129:084102
88. Stock G, Thoss M. 1997. Semiclassical description of nonadiabatic quantum dynamics. *Phys. Rev. Lett.* 78:578–81
89. Stock G, Thoss M. 1999. Mapping approach to the semiclassical description of nonadiabatic quantum dynamics. *Phys. Rev. A* 59:64–79
90. Miller WH, McCurdy CW. 1978. Classical trajectory model for electronically nonadiabatic collision phenomena. A classical analog for electronic degrees of freedom. *J. Chem. Phys.* 69:5163–73
91. Meyer H-D, Miller WH. 1979. A classical analog for electronic degrees of freedom in nonadiabatic collision processes. *J. Chem. Phys.* 70:3214–23
92. Herman MF, Kluk E. 1984. A semiclassical justification for the use of non-spreading wavepackets in dynamics calculations. *Chem. Phys.* 91:27–34
93. Miller WH. 2002. An alternate derivation of the Herman–Kluk (coherent state) semiclassical initial value representation of the time evolution operator. *Mol. Phys.* 100:397–400
94. Bonella S, Coker DF. 2003. Semiclassical implementation of the mapping Hamiltonian approach for nonadiabatic dynamics using focused initial distribution sampling. *J. Chem. Phys.* 118:4370–85
95. Bonella S, Coker DF. 2005. LAND-map, a linearized approach to nonadiabatic dynamics using the mapping formalism. *J. Chem. Phys.* 122:194102
96. Bonella S, Montemayor D, Coker DF. 2005. Linearized path integral approach for calculating nonadiabatic time correlation functions. *PNAS* 102:6715–19
97. Makri N. 2011. Forward–backward semiclassical and quantum trajectory methods for time correlation functions. *Phys. Chem. Chem. Phys.* 13:14442–52
98. Poulsen JA, Nyman G, Rossky PJ. 2003. Practical evaluation of condensed phase quantum correlation functions: a Feynman–Kleinert variational linearized path integral method. *J. Chem. Phys.* 119:12179–93
99. Poulsen JA, Nyman G. 2004. Determination of the Van Hove spectrum of liquid He(4): an application of the Feynman–Kleinert linearized path integral methodology. *J. Phys. Chem. A* 108:8743–51
100. Poulsen JA, Nyman G, Rossky PJ. 2005. Static and dynamic quantum effects in molecular liquids: a linearized path integral description of water. *PNAS* 102:6709–14
101. Shi Q, Geva E. 2003. Semiclassical theory of vibrational energy relaxation in the condensed phase. *J. Phys. Chem. A* 107:9059–69
102. Shi Q, Geva E. 2004. Nonradiative electronic relaxation rate constants from approximations based on linearizing the path-integral forward–backward action. *J. Phys. Chem. A* 108:6109–16

103. Shi Q, Geva E. 2003. Vibrational energy relaxation rate constants from linear response theory. *J. Chem. Phys.* 118:7562–71
104. Hsieh C-Y, Kapral R. 2012. Nonadiabatic dynamics in open quantum–classical systems: forward–backward trajectory solution. *J. Chem. Phys.* 137:22A507
105. Hsieh C-Y, Kapral R. 2013. Analysis of the forward–backward trajectory solution for the mixed quantum–classical Liouville equation. *J. Chem. Phys.* 138:134110
106. Kapral R. 2015. Quantum dynamics in open quantum–classical systems. *J. Phys. Condens. Matter* 27:073201
107. Dunkel ER, Bonella S, Coker DF. 2008. Iterative linearized approach to nonadiabatic dynamics. *J. Chem. Phys.* 129:114106
108. Davydov AS. 1971. *Theory of Molecular Excitons*. New York: Plenum
109. Olbrich C, Jansen TLC, Liebers J, Aghtar M, Strümpfer J, et al. 2011. From atomistic modeling to excitation transfer and two-dimensional spectra of the FMO light-harvesting complex. *J. Phys. Chem. B* 115:8609–21
110. Cole DJ, Chin AW, Hine NDM, Haynes PD, Payne MC. 2013. Toward ab initio optical spectroscopy of the Fenna–Matthews–Olson complex. *J. Phys. Chem. Lett.* 4:4206–12
111. Gao J, Shi W-J, Ye J, Wang X, Hirao H, Zhao Y. 2013. QM/MM modeling of environmental effects on electronic transitions of the FMO complex. *J. Phys. Chem. B* 117:3488–95
112. List NH, Curutchet C, Knecht S, Mennucci B, Kongsted J. 2013. Toward reliable prediction of the energy ladder in multichromophoric systems: a benchmark study on the FMO light-harvesting complex. *J. Chem. Theory Comput.* 9:4928–38
113. Hayes D, Engel GS. 2011. Extracting the excitonic Hamiltonian of the Fenna–Matthews–Olson complex using three-dimensional third-order electronic spectroscopy. *Biophys. J.* 100:2043–52
114. Raszewski G, Saenger W, Renger T. 2005. Theory of optical spectra of photosystem II reaction centers: location of the triplet state and the identity of the primary electron donor. *Biophys. J.* 88:986–98
115. Raszewski G, Diner BA, Schlodder E, Renger T. 2008. Spectroscopic properties of reaction center pigments in photosystem II core complexes: revision of the multimer model. *Biophys. J.* 95:105–19
116. Novoderezhkin VI, Romero E, Dekker JP, van Grondelle R. 2011. Multiple charge-separation pathways in photosystem II: modeling of transient absorption kinetics. *ChemPhysChem* 12:681–88
117. Novoderezhkin VI, Dekker JP, van Grondelle R. 2007. Mixing of exciton and charge-transfer states in photosystem II reaction centers: modeling of Stark spectra with modified Redfield theory. *Biophys. J.* 93:1293–311
118. Krueger BP, Scholes GD, Fleming GR. 1998. Calculation of couplings and energy-transfer pathways between the pigments of LH2 by the ab initio transition density cube method. *J. Phys. Chem. B* 102:5378–86
119. Madjet ME, Abdurahman A, Renger T. 2006. Intermolecular Coulomb couplings from ab initio electrostatic potentials: application to optical transitions of strongly coupled pigments in photosynthetic antennae and reaction centers. *J. Phys. Chem. B* 110:17268–81
120. Rätsep M, Freiberg A. 2007. Electron–phonon and vibronic couplings in the FMO bacteriochlorophyll *a* antenna complex studied by difference fluorescence line narrowing. *J. Lumin.* 127:251–59
121. Wendling M, Pullerits T, Przyjalowski MA, Vulto SIE, Aartsma TJ, et al. 2000. Electron–vibrational coupling in the Fenna–Matthews–Olson complex of *Prosthecochloris aestuarii* determined by temperature-dependent absorption and fluorescence line-narrowing measurements. *J. Phys. Chem. B* 104:5825–31
122. Kell A, Feng X, Reppert M, Jankowiak R. 2013. On the shape of the phonon spectral density in photosynthetic complexes. *J. Phys. Chem. B* 117:7317–23
123. Nitzan A. 2006. *Chemical Dynamics in Condensed Phases*. New York: Oxford Univ. Press
124. Lee M, Coker DF. 2016. Modeling electronic–nuclear interactions for excitation energy transfer in light-harvesting. *J. Phys. Chem. Lett.* Submitted
125. Moret M-E, Tavernelli I, Rothlisberger U. 2009. Combined QM/MM and classical molecular dynamics study of [Ru(bpy)₃]²⁺ in water. *J. Phys. Chem. B* 113:7737–44
126. Laino T, Mohamed F, Laio A, Parrinello M. 2005. An efficient real space multigrid QM/MM electrostatic coupling. *J. Chem. Theory Comput.* 1:1176–84

127. Ananth N, Venkataraman C, Miller WH. 2007. Semiclassical description of electronically nonadiabatic dynamics via the initial value representation. *J. Chem. Phys.* 127:084114
128. Wang H, Thoss M, Sorge KL, Gelabert R, Giménez X, Miller WH. 2001. Semiclassical description of quantum coherence effects and their quenching: a forward-backward initial value representation study. *J. Chem. Phys.* 114:2562-71
129. Huo P, Miller TF III, Coker DF. 2013. Predictive partial linearized path integral simulation of condensed phase electron transfer dynamics. *J. Chem. Phys.* 139:151103
130. Huo P, Miller TF. 2015. Electronic coherence and the kinetics of inter-complex energy transfer in light-harvesting systems. *Phys. Chem. Chem. Phys.* 17:30914-24
131. Caruso F, Chin AW, Datta A, Huelga SF, Plenio MB. 2009. Highly efficient energy excitation transfer in light-harvesting complexes: the fundamental role of noise-assisted transport. *J. Chem. Phys.* 131:105106
132. Chin AW, Datta A, Caruso F, Huelga SF, Plenio MB. 2010. Noise-assisted energy transfer in quantum networks and light-harvesting complexes. *New J. Phys.* 12:065002
133. Rebentrost P, Mohseni M, Aspuru-Guzik A. 2009. Role of quantum coherence and environmental fluctuations in chromophoric energy transport. *J. Phys. Chem. B* 113:9942-47
134. Rebentrost P, Mohseni M, Kassal I, Lloyd S, Aspuru-Guzik A. 2009. Environment-assisted quantum transport. *New J. Phys.* 11:033003
135. Cao J, Silbey RJ. 2009. Optimization of exciton trapping in energy transfer processes. *J. Phys. Chem. A* 113:13825-38
136. Ishizaki A, Fleming GR. 2011. On the interpretation of quantum coherent beats observed in two-dimensional electronic spectra of photosynthetic light harvesting complexes. *J. Phys. Chem. B* 115:6227-33
137. Nalbach P, Thorwart M. 2012. The role of discrete molecular modes in the coherent exciton dynamics in FMO. *J. Phys. B* 45:154009
138. Kelly A, Brackbill NJ, Markland TE. 2015. Accurate nonadiabatic quantum dynamics on the cheap: making the most of mean field theory with master equations. *J. Chem. Phys.* 142:094110
139. O'Reilly EJ, Olaya-Castro A. 2014. Non-classicality of the molecular vibrations assisting exciton energy transfer at room temperature. *Nat. Comm.* 5:3012
140. Heyd J, Scuseria GE, Ernzerhof M. 2003. Hybrid functionals based on a screened Coulomb potential. *J. Chem. Phys.* 118:8207-15
141. Higashi M, Kosugi T, Hayashi S, Saito S. 2014. Theoretical study on excited states of bacteriochlorophyll *a* in solutions with density functional assessment. *J. Phys. Chem. B* 118:10906-18
142. Mühlbacher L, Kleinekathöfer U. 2012. Preparational effects on the excitation energy transfer in the FMO complex. *J. Phys. Chem. B* 116:3900-6
143. McKemmish LK, McKenzie RH, Hush NS, Reimers JR. 2011. Quantum entanglement between electronic and vibrational degrees of freedom in molecules. *J. Chem. Phys.* 135:244110
144. Wu J, Tang Z, Gong Z, Cao J, Mukamel S. 2015. Minimal model of quantum kinetic clusters for the energy-transfer network of a light-harvesting protein complex. *J. Phys. Chem. Lett.* 6:1240-45
145. Ritschel G, Roden J, Strunz WT, Aspuru-Guzik A, Eisfeld A. 2011. Absence of quantum oscillations and dependence on site energies in electronic excitation transfer in the Fenna-Matthews-Olson trimer. *J. Phys. Chem. Lett.* 2:2912-17
146. Ritschel G, Roden J, Strunz WT, Eisfeld A. 2011. An efficient method to calculate excitation energy transfer in light-harvesting systems: application to the Fenna-Matthews-Olson complex. *New J. Phys.* 13:113034
147. Schmidt am Busch M, Müh F, Madjet ME-A, Renger T. 2011. The eighth bacteriochlorophyll completes the excitation energy funnel in the FMO protein. *J. Phys. Chem. Lett.* 2:93-98



Contents

The Independence of the Junior Scientist's Mind: At What Price? <i>Giacinto Scoles</i>	1
Vacuum Ultraviolet Photoionization of Complex Chemical Systems <i>Oleg Kostko, Biswajit Bandyopadhyay, and Musabid Ahmed</i>	19
Real-Time Probing of Electron Dynamics Using Attosecond Time-Resolved Spectroscopy <i>Krupa Ramasesha, Stephen R. Leone, and Daniel M. Neumark</i>	41
Charge-Carrier Dynamics in Organic-Inorganic Metal Halide Perovskites <i>Laura M. Herz</i>	65
Vibrational Control of Bimolecular Reactions with Methane by Mode, Bond, and Stereo Selectivity <i>Kopin Liu</i>	91
Interfacial Charge Transfer States in Condensed Phase Systems <i>Koen Vandewal</i>	113
Recent Advances in Quantum Dynamics of Bimolecular Reactions <i>Dong H. Zhang and Hua Guo</i>	135
Enhancing Important Fluctuations: Rare Events and Metadynamics from a Conceptual Viewpoint <i>Omar Valsson, Pratyush Tiwary, and Michele Parrinello</i>	159
Vibrational Heat Transport in Molecular Junctions <i>Dvira Segal and Bijay Kumar Agarwalla</i>	185
Gas-Phase Femtosecond Particle Spectroscopy: A Bottom-Up Approach to Nucleotide Dynamics <i>Vasilios G. Stavros and Jan R.R. Verlet</i>	211
Geochemical Insight from Nonlinear Optical Studies of Mineral-Water Interfaces <i>Paul A. Covert and Dennis K. Hore</i>	233

Charge Transfer Dynamics from Photoexcited Semiconductor Quantum Dots <i>Haiming Zhu, Ye Yang, Kaifeng Wu, and Tianquan Lian</i>	259
Valence Electronic Structure of Aqueous Solutions: Insights from Photoelectron Spectroscopy <i>Robert Seidel, Bernd Winter, and Stephen E. Bradforth</i>	283
Molecular Shape and the Hydrophobic Effect <i>Matthew B. Hillyer and Bruce C. Gibb</i>	307
Characterizing Localized Surface Plasmons Using Electron Energy-Loss Spectroscopy <i>Charles Cherqui, Niket Thakkar, Guoliang Li, Jon P. Camden, and David J. Masiello</i>	331
Computational Amide I 2D IR Spectroscopy as a Probe of Protein Structure and Dynamics <i>Mike Reppert and Andrei Tokmakoff</i>	359
Understanding the Surface Hopping View of Electronic Transitions and Decoherence <i>Joseph E. Subotnik, Amber Jain, Brian Landry, Andrew Petit, Wenjun Ouyang, and Nicole Bellonzi</i>	387
On the Nature of Bonding in Parallel Spins in Monovalent Metal Clusters <i>David Danovich and Sason Shaik</i>	419
Biophysical Insights from Temperature-Dependent Single-Molecule Förster Resonance Energy Transfer <i>Erik D. Holmstrom and David J. Nesbitt</i>	441
Next-Generation Force Fields from Symmetry-Adapted Perturbation Theory <i>Jesse G. McDaniel and J.R. Schmidt</i>	467
Measuring the Hydrodynamic Size of Nanoparticles Using Fluctuation Correlation Spectroscopy <i>Sergio Dominguez-Medina, Sishan Chen, Jan Blankenburg, Pattanawit Swanglap, Christy F. Landes, and Stephan Link</i>	489
Atomic and Molecular Collisions at Liquid Surfaces <i>Maria A. Tesa-Serrate, Eric J. Smoll Jr., Timothy K. Minton, and Kenneth G. McKendrick</i>	515
Theory of Linear and Nonlinear Surface-Enhanced Vibrational Spectroscopies <i>Dhabih V. Chulbai, Zhongwei Hu, Justin E. Moore, Xing Chen, and Lasse Jensen</i>	541

Single-Molecule Studies in Live Cells <i>Ji Yu</i>	565
Excited-State Properties of Molecular Solids from First Principles <i>Leeor Kronik and Jeffrey B. Neaton</i>	587
Water-Mediated Hydrophobic Interactions <i>Dor Ben-Amotz</i>	617
Semiclassical Path Integral Dynamics: Photosynthetic Energy Transfer with Realistic Environment Interactions <i>Mi Kyung Lee, Pengfei Huo, and David F. Coker</i>	639
Reaction Coordinates and Mechanistic Hypothesis Tests <i>Baron Peters</i>	669
Fundamental Properties of One-Dimensional Zinc Oxide Nanomaterials and Implementations in Various Detection Modes of Enhanced Biosensing <i>Jong-in Hahn</i>	691
Liquid Cell Transmission Electron Microscopy <i>Hong-Gang Liao and Haimei Zheng</i>	719

Indexes

Cumulative Index of Contributing Authors, Volumes 63–67	749
Cumulative Index of Article Titles, Volumes 63–67	753

Errata

An online log of corrections to *Annual Review of Physical Chemistry* articles may be found at <http://www.annualreviews.org/errata/physchem>